Correlation analysis between cationic metal characteristics and ion-exchange performance of brick-derived zeolites: A comprehensive mechanistic explanation

O. Allahdin, N. Poumaye, M. Wartel, A. Boughriet

To cite this version:

O. Allahdin, N. Poumaye, M. Wartel, A. Boughriet. Correlation analysis between cationic metal characteristics and ion-exchange performance of brick-derived zeolites: A comprehensive mechanistic explanation. Materials Chemistry and Physics, 2021, 276, pp.125353. 10.1016/j.matchemphys.2021.125353 . hal-03557645

HAL Id: hal-03557645
https://hal.science/hal-03557645v1

Submitted on 5 Jan 2024

CORRELATION ANALYSIS BETWEEN CATIONIC METAL CHARACTERISTICS AND ION-EXCHANGE PERFORMANCE OF BRICK-DERIVED ZEOLITES: A COMPREHENSIVE MECHANISTIC EXPLANATION

O. Allahdin[a,b], N. Poumaye[a,b], M. Wartel[a], A. Boughriet[a*].

[a]. Université Lille, Laboratoire LASIR (UMR CNRS 8516), Equipe Physico-chimie de l'Environnement. Bât. C8 2ème étage, 59655 Villeneuve d'Ascq cedex, France.

[b]. Chaire Unesco « Sur la gestion de l'eau », Laboratoire Hydrosciences Lavoisier, Université de Bangui, Faculté des Sciences, B.P. 908, République Centrafricaine.

* Corresponding author. Fax: E-mail: abdel.boughriet@univ-lille.fr (A. Boughriet)
Université Lille, Laboratoire LASIR (UMR CNRS 8516), Equipe Physico-chimie de l'Environnement. Bât. C8 2ème étage, 59655 Villeneuve d'Ascq cedex, France.

ABSTRACT

A metakaolinite-rich brick originated from Central African Republic was modified with sodium hydroxide according to a zeolitization process. The synthesized material was characterized by means of environmental scanning electron microscopy and X-ray diffraction. Pore size distribution was determined by nitrogen adsorption-desorption analysis. The equilibrium reactions between the Na-exchanged forms of brick-derived zeolites and aqueous solutions containing one, two or three cationic metals ($Me^{2+} = Cd^{2+}$, Fe^{2+}, Ni^{2+} and Pb^{2+}) were studied in the batch mode at room temperature. Experimental equilibrium results were plotted in the form of "ion-exchange isotherms" in order to better interpret data in terms of metals affinity /selectivity. Kielland plots were drawn and thermodynamic equilibrium constant and standard Gibbs free energy were determined for each $2Na^+ \rightarrow Me^{2+}$ or $Me_1^{2+} \rightarrow Me_2^{2+}$ exchange. Thermodynamic data were analyzed on the basis of both the general properties of divalent metals in water and the surface behavior of the brick.These investigations permitted to show the importance of *first* hydrated radius, ionic potential and hydration free energy and *second* kinetics and mass-transfer/diffusion on the course of the ion-exchange process at brick-water interface.

Keywords: brick; zeolite; heavy metal; ion exchange; selectivity; thermodynamics.

1. Introduction

Heavy metals have been extensively employed in various industrial processes, leading to elevated discharges of metals into aqueous environments. Heavy metal ions, for instance Cd^{2+}, Ni^{2+}, and Pb^{2+}, are among the most common toxic pollutants found in wastewaters, and hence, can pose with time serious threats to aquatic organisms and human health if no strict controls of hazardous industrial effluents are made rapidly. Unfortunately, the amount of these heavy metals which are discharged into aquatic media continues to increase. With the increase in heavy metal pollution and stricter emissions standards worldwide, there is a pressing need for the development of novel methods to obtain potable water by respecting permissible limits of metals in drinking water which are fixed by international and national guidance agencies.

Ferrous ion was added to the list of cationic metals studied here because of its high levels in numerous anoxic ground waters which were commonly used as drinking water by local population in developing counties. Thus, in Central African Republic (in Bangui region), the content of soluble iron in ground waters is around 5 ppm and sometimes up to or even >10 ppm) [1]. These values exceed largely the permissible limit recommended by the World Health Organization (WHO), *i.e.*: 0.3mg.L^{-1} [2]. Note also that ferrous ion is oxidized progressively by atmospheric oxygen to give ferric iron, Fe(III), which subsequently precipitates as colloidal iron oxide/hydroxide. Such a precipitation is responsible for domestic issues such as reddish colour, staining of laundry, and solids deposition in the water leading to high turbidity. Furthermore, the atmospheric oxidation of ferrous ions present in ground waters leads to the growth of bacterial micro-organisms. These bacterial proliferations are responsible with time for bad odour and an increase of unpleasant taste [3, 4], and also for serious domestic problems such as cloggings of pipes and softeners [5, 6], and even punctures and leakages in the water distribution system [3, 4, 7]. It is further worth noting that accumulation of iron in human body can cause with time grave diseases such as eye disorders, or even heart and cancer [8-14].

The elimination of hazardous industrial materials can be made from adequate treatments such as precipitation, membrane separation, electrochemical method, adsorption and ion-exchange [15, 16]. Generally, ion-exchange / adsorption processes occur more efficiently and, in addition, they are easier to be implemented. These processes necessitate the use of natural products (agricultural by-products, woody materials and wastes [17] or synthetic materials [15]. However, their cost and complex or expensive regeneration / maintenance procedures have nevertheless to be evaluated before using them for treating polluted waters. This explains why in developing countries more attention has been given specifically to local materials with high efficiency and low cost for removing heavy metals from waste-waters.

Recent works showed that natural or synthesized zeolites can possess high ability for ion-exchange / adsorption of cationic metals, ***e.g.***: the removal of nickel(II) by Jordan natural zeolite [18]; Ag^+, Cu^{2+}, and Co^{2+} ions by faujasite zeolite Y [19]; and Cu^{2+} and Pb^{2+} by zeolite-Y [20]. Nevertheless, their application for water treatment at large scale might pose some problems when passing contaminated solutions through pilot systems because of difficult filtrations and high-pressure drops. Recently, various natural minerals (***e.g.,*** loess) and alumino-silicate waste materials (***e.g.***, coal fly ash) were transformed into zeolites-based composites and used successfully for heavy metal removal [21, 22]. Such *zeolite-based composites* made at low-cost offered instead good chelating / selectivity/ reusability and sufficiently high kinetic rate for water treatment [23].

In the past, the brick material had frequently been utilized as a low–cost adsorbent or exchanger for removing metals like: Hg(II) [24]; Zn(II) [25]; Cr(VI) [26]; both Cr(VI) and Ni(II) [27]; or Ni(II) alone [28]. Note further that a brick made in Central African Republic was also found to be a particular good adsorbent for the removals of heavy metals (such as: Cd^{2+}, Fe^{2+}, Pb^{2+} and Zn^{2+}) from aqueous solutions after HCl treatment of the material followed by a coating with ferrihydrite solutions [29- 35]. This brick is made craftily in Bangui region from local soils. These latter contain high proportions of kaolinite (20-25 w%) and sand (60-65 w%) and, to a lesser extent, other minerals like: illite, rutile and iron oxihydroxides [29]. Thermal treatment of Bangui soils was carried out craftily in charcoal ovens at temperature varying from 600 to 750°C, allowing the conversion of kaolinite ($Al_2O_3.2SiO_2.2H_2O$) into metakaolinite ($Al_2O_3.2SiO_2$).

Because of the low Si/Al atomic ratio in metakaolinite (close to 1), this mineral is considered as an ideal alumino-silicate and strongly recommended in the recent literature as a convenient starting material for the synthesis of low-silica zeolites such as zeolite A and zeolite P [36-38]. In recent works [39], Bangui brick had been treated with sodium hydroxide in order to generate alkali brick as *zeolite-based composite* containing low-silica zeolites. The general chemical formula of these brick-derived zeolites can be written as [40, 41]:

$(Na^+)_x(AlO_2^-)_x.(SiO_2)_y.\ zH_2O$ (1);

where x and y correspond to the number of “AlO_4” and “SiO_4” tetrahedra per crystallographic unit cell, respectively; and z the number of water molecules per unit cell. The chemical formula leads to negative charges (x-) which are balanced by extra framework cations (Na^+ ions with total positive charges: x+). The x/y ratio in formula (1) is maximal according to the well-known Lönwenstein’s rule [42], thus explaining the rich ion-exchange chemistry of this composite. In the lab, brick-derived zeolites were tested as ion exchangers and experimental data revealed their excellent ability to remove metallic contaminants from aqueous solution [1, 43-45].

The first objective of this research was to undertake the zeolitization of Bangui brick and to characterize the resulting material by conducting environmental scanning electron microscopy (ESEM) and X-ray diffraction (XRD) and porosity measurements. The second objective was to perform ion-exchange reactions between the modified brick and the cationic metals: Cd^{2+}, Fe^{2+}, Ni^{2+} and Pb^{2+} (in single and binary-metals systems) and to determine ion-exchange isotherms and corresponding thermodynamic equilibrium constants by using Kielland plots. The third objective was to identify physical, chemical and/or kinetic parameters which were susceptible to govern the thermodynamics of the process and selectivity sequence.

2. Materials and methods

2.1. Synthesis and characterization

The raw material used in the experiments was obtained from a brick made locally by craftsmen in Bangui region (Central African Republic). The brick was broken into grains and seized and the 0.7-1.0 mm fraction was selected. 10 g of this fraction were put inside a closed Teflon flask and treated with 40 mL of sodium hydroxide ($0.6 mol.L^{-1}$) at room temperature for one night under slow shaking at a speed of 120 rpm. This procedure was afterwards followed by a fixed-temperature increase of the mixture at 90°C for a constant reaction time of six days. The recovered grains were afterwards rinsed several times with MilliQ water and dried at 90°C for 24 hours. The mineralogical composition of the modified brick was obtained using X-ray diffraction and scanning electron microscopy.

2.2. Chemicals

All chemicals employed in the experiments were analytical grades. Sodium hydroxide Dislab (France), $Pb(NO_3)_2$ Fisher Chemical; $Cd(NO_3)_2.4H_2O$; $Ni(NO_3)_2.6H_2O$; and $FeCl_2.4H_2O$ were supplied by DISLAB (France).

2.3. ICP-AES analyses

Recovered solutions were analyzed for element contents using ICP-AES (Inductively Coupled Plasma – Atomic Emission Spectroscopy; model Varian Pro Axial View).

2.4. Fixed-bed column experiments

In order to apply our water-treatment method in the field, it had been necessary to undertake preliminarily complementary and systematic studies on the modified brick under dynamic conditions (i.e., in fixed-bed column) [46]. In this work, the effects of the variable bed depth, flow rate and column diameter on the metal uptake at brick surfaces were examined in details in the aim to optimize the different physical parameters involved. Thus, bed depth service time (BDST) model was used successfully for assessing the column capacity, and breakthrough data predictions indicated good agreement with experimental data. In addition, at a bed height of 10-7.5cm the critical bed depth was determined (ranging from 4.7 to 4.9cm at a flow rate of $2.5mL.min^{-1}$ and from 6 to 7cm at a flow rate of $7.5\text{-}10.0\ mL.min^{-1}$). And finally, the Thomas model was successfully employed to fit brick-column results at various flow rates.

As for the effect of the material particle size, it was optimized by using brick grains with diameter sizes ranging from 0.7 to 1.0 mm in the aim to obtain better flow rate and permeability through fixed-bed columns and also a contact time sufficient for assuring ideally the ion-exchange process. In addition, the presence of sand (60-65 wt%) in this material assures as well a good permeability and facilitates the flow of water through brick beds.

Continuous flow ion-exchange experiments were conducted in a fixed-bed glass column with an inner diameter of 12.5 mm, a height of 25 cm, and a medium porosity sintered-pyrex disk at its bottom in order to prevent any loss of material. A bed depth of 8.5 cm (10.0 - 10.5 g) was investigated at a constant flow rate of 10mLmin^{-1}. This height of bed depth was chosen to be higher than the critical bed depth.

In order to fix the influent metal concentration in column experiments, we took into consideration the elevated levels of soluble iron in certain ground-waters in Central African Republic source [1], which were deemed unsafe and often found to be much above the maximum permissible limit recommended by the WHO [47], ***i.e.***: 300 µg.L^{-1}. Indeed, the maximum Fe^{2+} ions concentration in some Bangui ground-waters can attain up to 10mg.L^{-1} or 1.79x10^{-4} mol.L^{-1}. Such water sources should then pose a serious threat locally to human health when consumed untreated. In what follows, for column experiments we then decided to fix the influent iron(II) concentration at 1.79x10^{-4} mol.L^{-1}. The same metal concentration was also used for removing Cd^{2+}, Ni^{2+} and Pb^{2+} ions in single-metal column systems, knowing further that their permissible limit recommended by the WHO was largely much lower than that for Fe^{2+} ions (Cd: 3µg.L^{-1}; Ni: 70 µg.L^{-1}; and Pb: 10 µg.L^{-1} [47]).

The metal solution was pumped through the column at a desired flow rate by means of a peristaltic pump (Modern Labo France Type KD1170) in a down-flow mode. During this column experiment, pH was measured continuously at room temperature, and effluent samples exiting the bottom of the column were collected at different time intervals and analyzed for metal contents by using ICP-AES.

The flow to the column was continued until the effluent metal concentration at time t (C_t) reached the influent metal concentration (C_o): $C_t/C_o \approx 0.98$. The performance of packed bed was described in the present work through the concept of the breakthrough curve. To access the ion-exchange performance of alkali brick, the breakthrough time (t_b) and the exhaustive time (t_e) were determined under given operational conditions. They were defined as the elapsed time values when the effluent metal concentration (C_t) attained 5% (t_b) and 90% (t_e) of the influent metal concentration (C_o).

2.5. Ion-exchange (batch) experiments

Ion-exchange experiments were conducted at room temperature for the binary (1:2) –ion-exchange systems (Na^+, Me^{2+}): Na^+/Cd^{2+}; Na^+/Fe^{2+}; Na^+/Ni^{2+}; and Na^+/Pb^{2+} by equilibrating a weighed amount of alkali brick (0.5 g of brick pellets with average diameters varying from 0.7 to 1.0 mm) with solutions of Na^+ and Me^{2+} ions (50mL) at a total cation normality of 0.01 eq.L^{-1} (or 0.01N). The 0.01eq.L^{-1}solutions were prepared from a solution of $NaNO_3$ salt ($[Na^+]$ = 0.01mol.L^{-1}) and a solution of metal salt ($[Me^{2+}]$ = 0.005mol.L^{-1} or 0.01eq.L^{-1}). We employed the following reagent grade compounds: $NaNO_3$; $Cd(NO_3)_2.4H_2O$; $Ni(NO_3)_2.6H_2O$; $FeCl_2.4H_2O$; and $Pb(NO_3)_2$. For each binary system (Na^+, Me^{2+}), we prepared up to 14 aqueous mixtures of Na^+ and Me^{2+} cations in which the individual cationic normality of each of these ions ranged from 0.00 to 0.01eq.L^{-1} (with $[Na^+] + 2[Me^{2+}] = 0.01$ molL^{-1}).

On the other hand, it was previously shown that the Na^+/Me^{2+} exchange process was rapid and the time to reach the equilibrium state was about 4 hours [45]. Thereby, for all the ion-exchange experiments performed here we decided to fix arbitrarily the reaction time at 24 hours. The different suspensions were then continuously and gingerly mixed at the fixed reaction time, allowing the $2Na^+ \rightarrow Me^{2+}$ exchange to reach the equilibrium state. At the beginning and end of ion-exchange experiments, pH was measured. The resulting supernatants were filtered through a 0.45 μm pore diameter (cellulose nitrate filter) and analyzed for the determination of sodium and metal levels by ICP-AES.

2.6. Electron Microscopy analysis

Micrographies of representative specimens of alkali brick were recorded by using an environmental scanning electron microscope (ESEM, Quanta 200 FEI). Elemental analysis was performed using ESEM/EDS (ESEM, model: QUANTA–200–FEI, equipped with an Energy Dispersive X-Ray Spectrometer EDS X flash 3001 and monitored by QUANTA–400 software elaborated by Bruker). EDS measurements were carried out at 20 kV at low vacuum (1.00 Torr) and the maximum pulse throughput was 20 kcps. Different surface areas ranging from 0.5 to 3.5 mm² were targeted on alkali-brick grains and examined by ESEM/EDS. For that, a narrow beam scanned selected areas of brick pellets for chemical analysis. Atomic quantifications and mathematical treatments were undertaken using QUANTA-400 software in order to determine the averaged elemental composition of the surface brick and to detect chemical / elemental variabilities.

2.7. X-ray diffraction analysis

XRD patterns were conducted at room temperature in a Bruker D8 Advance diffractometer using Ni-filtered CuKα radiation (40kV, 40 mA). Samples were scanned with a step size of 0.02° and a counting time of 0.5 sec per step

2.8. Nitrogen adsorption-desorption isotherms

The textural characterization of brick samples was determined from the N_2 adsorption desorption isotherm at 77 K by using Sorptomatic 1990 Carlo Erba. The specific superficial area was assessed by the Brunauer-Emmet -Teller (BET) method. The pore volume was estimated by the α-plot method. Total pore volume was evaluated from desorption isotherm branch at P/Po = 0.98 assuming complete pore saturation. Pore size distribution was calculated by Non-Local Density Functional Theory (NLDFT) and Berrett Joyner Halenda (BJH) method.

3. Results

3.1. Characterization of brick samples

3.1.1. X-ray diffraction analysis

Fig. 1A exemplifies the XRD patterns of raw-brick powder. The results showed that the material contains quartz as the principal crystalline mineral and, to a lesser extent, illite and rutile. Quartz was identified on the basis of the following ‘2θ’ reflection angles (the Miller indices, hkl, are given in the parenthesis): 20.9° (100); 26.6° (011); 36.5° (110); 39.5° (102); 40.3° (111); 42.4° (200); 45.8° (201); and 50.1° (112) [ICSD Collection Code: 89276]. Because of the smaller amounts of illite and rutile in the brick, these two minerals were recognized only on the basis of some of their intensive reflection angles: ***illite***: 8.8° (001), 17.9° (004), 19.8° (021), and 34.3° (034) [ICDD (International Centre for Diffraction data): 00-009-0343]; ***rutile***: 27.4° (110) and 36.1° (101) [ICSD Collection Code: 168140]. Dehou and his coworkers [29] further evidenced the presence of metakaolinite in the brick made in Bangui region. The XRD pattern of the calcined kaolinite (metakaolinite) resembles enough to that of an amorphous material [48]. The XRD diffractogram exhibits a very broad featureless band extending from approximately 20° to 40° 2θ (Cu Kα), with a maximum at about 30° 2θ [49]. Note, however, that this broad signal can hardly be observed in the XRD diffractogram of the brick because, in this composite quartz is the major compound (> 60 w%) and metakaolinite represents no more than 30w%.

Fig. 1B exemplifies the XRD patterns of alkali-brick powder. The results indicated the appearance of new signals in addition to those ascribed to quartz, illite and rutile. These new peaks were attributed to zeolites LTA and NaP. The distinguishing peaks of zeolite LTA at $2\theta = 7.2°$, 10.2°, 12.5° and 21.7° can be imputed to lattice plans of (200), (220), (222) and (600 and 442), respectively [50]. The distinguishing peaks of zeolite NaP at $2\theta = 12.5°$, 17.7°, 21.7°, 28.1°, 33.4° and 46.1° can be imputed to lattice plans of (101 and 110), (200 and 002), (211, 112 and 121), (310, 301, and 103), (132, 123, 231, 213, 312, and 321) and (134), respectively [50].

3.1.2. Scanning electron microscopy analysis

The ESEM micrograph of raw brick exhibits porous and non-uniform textural surfaces with major fissures and cracks, except for quartz crystals (Fig. 2A). Semi-quantitative ESEM/EDS analysis was performed on various brick particles. Globally, ESEM/EDS data revealed the occurrence of: (i) silicon (Si), aluminum (Al), oxygen (O) and iron (Fe) as major elements; and (ii) titanium (Ti), magnesium (Mg), potassium (K), calcium (Ca) and sodium (Na) as minor elements. In order to obtain the spatial distribution of these elements, EDS mapping scanning was afterwards performed on the brick-particles region shown in Fig. 2B. The reconstituted EDS mapping image (Fig. 2B) revealed that the elements Al, Si, and Fe are distributed across brick surfaces with apparent localizations: silicon-rich crystalline forms (*in blue*), (Al, Si)-rich particles (*in violet*) and iron-rich aggregates (*in green*). This chemical spatial/micro-analysis of the brick confirmed the presence of SiO_2 (quartz), alumino-silicate (which was previously identified as metakaolinite [29] with the chemical formulae: $2SiO_2.Al_2O_3$) and iron oxides/hydroxides, respectively. The detection of K-rich specimens (*in blue light*) at low levels confirmed the existence of illite (with the chemical formulae: $[(K,H_3O)(Al,Mg,Fe)_2(Si,Al)_4O_{10}[(OH)_2,(H_2O)]]$).

After a chemical treatment of the brick with a 0.6molL^{-1}−NaOH solution at 90°C for 6 days, an ESEM micrograph of treated brick pellets was made (Fig. 3A). As seen in this figure, several broad targeted zones were analyzed by the ESEM/EDS technique in the aim to gain information about the averaged elemental composition at brick surfaces (for instance, Fig. 4 represents a typical EDS spectrum of a targeted brick zone shown in Fig 3A). We found: 69.98 ± 0.89 atomic % for oxygen; 10.97 ± 0.68 atomic% for aluminium; 17.29 ± 0.25 atomic % for silicon; 9.08 ± 0.25 atomic % for sodium; 0.50 ± 0.18 atomic % for iron; 0.37 ± 0.02 atomic % for magnesium; and 0.18 ± 0.05 for titanium. Note that for the Ti element, it was identified clearly by EDS analysis as titanium dioxide (TiO_2) in some micro-specimens which appeared in the ESEM images of both Fig. 2A (raw brick) and Fig. 3B (alkali brick) with very white tones. These analyses confirmed that this mineral was chemically very stable during the alkaline treatment. As pointed out previously [51], the low ion-exchange characteristics of raw brick (in which TiO_2 was present at very low amount, < 1w%) suggested that the TiO_2 mineral did not affect the ion-exchange process under study.

EDS data indicated clearly a significant increase of Na amount at the treated brick surface (0.50 ± 0.18 atomic %) in comparison with that on the raw brick (≤0.03 atomic %). Note also that, after NaOH treatment, noticeable modifications of the brick surface were observed by ESEM microscopy. Particularly, the surface morphology of the material changed significantly by the apparition of cubic and spherical micro-particles at brick surfaces (see Fig. 3B). Their sizes varied from 8 μm to 12 μm for cubic micro-specimens and from 3 μm to 8 μm for spherical micro-specimens. Quantitative ESEM/EDS analysis indicated that the elemental composition of these micro-specimens corresponded well enough to those of zeolites with atomic ratios Si:Al ≈1. We found: 14.77 ± 2.67 atomic % for sodium; 14.97 ± 2.05 atomic % for aluminium; and 16.12 ± 1.46 atomic % for silicon. The calculated atomic ratio Si/Al was then equal to about 1.08. The presence of high amounts of sodium on the surfaces of cubic and spherical particles confirmed the formation of Na-zeolites.

Recent works showed that, from the ESEM/EDS analyses of large regions of alkali-brick surfaces, roughly only two types of elements combinations predominated at these surfaces (when compared to raw-brick surfaces), namely: Si-O and Al-Si-Na [52]. These combinations were ascribed to quartz and zeolite, respectively. With this in mind, it had been possible to approximate the volumetric and mass percentage of quartz and zeolites present at the surface of the alkali-brick composite. We found: 30.72-36.71 volumetric % for zeolites and 63.29-69.28 volumic % for quartz; and 32.14-38.25 mass % for zeolites and 61.75-67.86 mass % for quartz. These surface % values revealed a coating process and enrichment of brick minerals (mainly quartz) with zeolitic alumino-silicates which occurred as follow. During the alkaline treatment metakaolinite was transformed into geo-polymer gels followed by a slow germination, deposition and crystallization of these gels into zeolites LTA and NaP at the surfaces of quartz grains.

3.1.3. Nitrogen adsorption-desorption analysis

Pore size distribution curves of brick materials were determined by nitrogen adsorption-desorption analysis (Fig. 5). As seen in this figure, the most abundant pores are in the diameter range 170 − 210 Å and 190 − 230 Å for raw brick and alkali brick respectively, which are in meso-size range.

For raw brick, a broad pore size distribution pattern was observed with specific mesoporous surface characteristics (Fig. 5a). Calculated results obtained from N_2 adsorption-desorption isotherms permitted to reveal the involvement of pore diameters varying mostly from ~24 Å to ~500 Å, a BET surface area of 31.2 m^2g^{-1}, an average pore diameter of 160 Å (between 17 Å and ~1000 Å), and an average pore volume of 0.15 $cm^3.g^{-1}$.

As for alkali brick, its pore size distribution curve exhibited mesoporous surface properties as well, however, with the appearance of a peak corresponding to an increase of meso-pores between 37 and 40 Å (Fig. 5b). The presence of this new peak at lower diameters would result specifically from the transformation of metakaolinite into zeolites by sodium hydroxide. Average pore diameter, pore volume (between 17 Å and ~1000 Å) and BET surface area measured for this modified brick are: 94.5-112.4 Å, 0.048-0.063 $cm^3.g^{-1}$ and 15.4-17.3 $m^2.g^{-1}$, respectively. Although these values are lower than those found for raw brick, our researches had permitted to show that the particular meso-porosity of alkali brick played a relevant role in improving heavy-metals removals from aqueous solutions through adsorption / ion-exchange process [1, 43-45]. It was further noticed that the use of a composite like alkali brick (which is mainly composed of zeolites and sand) had been found to be better in the field (in Bangui region) for the conception of a pilot associated with an iron(II) contaminated drilling and equipped with 'manual' and/or 'electric' pumps [51]. Note also that it is possible to increase the BET surface area of alkali brick simply by employing initially brick grains with much lower diameters than those used in the present work (0.7 - 1.0 mm).

3.2. Column study

To gain information about the stoichiometric aspect of the ion-exchange mechanism on brick-derived zeolites, the Na^+/Ni^{2+} exchange reaction was examined under dynamic conditions. The experiment was carried out in continuous mode by means of a fixed-bed column packed with brick pellets (diameters varying from 0.7 mm to 1.0 mm). The breakthrough curve was obtained by plotting the nickel concentration in the effluent against either the total volume passing through the column or the experiment time (Fig. 6). The curves which represent the variations of the effluent pH and the concentration of column sodium(I) released in the solution *versus* the effluent volume are also displayed in Fig. 6. It should be noted that, during the course of the ion-exchange process, a gradual decrease of the pH from 9.59 to 6.88 (as shown in Fig. 6) occurred in the effluent. Under our operational conditions, the breakthrough time (t_b) and the exhaustive time (t_e) were equal to: $t_b \approx$ 90mn (or 850mL of effluent volume) and $t_e \approx$ 230mn (or 2300mL of effluent volume).

Moreover, the content of released Na was plotted against the amount of nickel bound to the brick with time (Fig. 7). As can be seen in this figure, the slope of the curve (which corresponds to the molar ratio $[Na^+]_{released/}[Ni^{2+}]_{exchanged}$) was found to be around 1.94 with a good correlation coefficient (R^2 = 0.9934), see Fig. 7. This suggested that the studied heterogeneous reaction took place according to a stoichiometric process where nearly two balancing ions (Na^+) in the sodic brick were replaced by one incoming ion (Ni^{2+}) from the solution. Therefore, the reaction for the Ni^{2+}--Na^+ system might be represented by the following equation:

$$2\,(Na^+)_Z + (Ni^{2+})_S \rightarrow (Ni)_Z + 2\,(Na^+)_S \qquad (2)$$

The symbols “s” and “z” refer to the solution phase and zeolite phase, respectively. The “stoichiometric” molar atomic ratio, Na/Ni, was assumed in this work to be the theoretical exchange capacity of brick zeolites. Note that similarly column studies relative to the Na^+/Cd^{2+}, Na^+/Pb^{2+} and Na^+/Fe^{2+} exchanges were previously performed [1, 43, 46], revealing as well molar atomic ratios Na/Me to be close enough to 2.

In order to assess the possibility for the reuse of alkali brick after column saturation and recovery of metal cations, the regeneration of the exchanger was also tested by our research group [1, 46]. In these works, a continuous mode investigation of column for desorption-adsorption was undertaken in either in single- or multi-metal systems. Metal(s) desorption was evaluated by applying different desorbing agents and the best eluent was found to be sodium chloride (1.5 $mol.L^{-1}$). Subsequently, before proceeding to a new ion-exchange experiment the column pH was increased by passing a 0.01 $mol.L^{-1}$ NaOH solution through the column. For instance, it was shown that after passing synthesized iron(II) waters through alkali-brick column, the material had still good removal ability after five regeneration cycles (with yields > 40%); and in addition, yield could be improved by increasing the NaOH concentration in the reagent used for regeneration [1].

Consequently, the strong effect of Na^+ ions in excess (when passing through the metal-saturated column) on metal binding indicated that Na(I) solutions could reverse metal binding. Hence, one might suggest the absence of covalent bondings (or inner-sphere complexes) formed between metal ions and active brick sites, ***i.e.***: $(>SO)_2Me$; but rather the generation of outer-sphere complexes like: $2{>}SO^-Me(H_2O)_z^{2+}$.

3.3. Batch studies

In batch experiments, measured pH values were found to be above the pH at the point of zero charge (PZC; $pH_{PZC} = 5.85 \pm 0.10$) [45]. This meant that the surface of the zeolitic brick was negatively charged, which was favourable for cation exchange through electrostatic attraction. On the other hand, the Visual MINTEQ 3.0 equilibrium speciation computer software was previously used to calculate the concentrations of the various metal species/hydroxyl complexes generated in the experimental reacting solution [45]. Metal-distribution graphs revealed clearly almost only free forms of metal ions (≥98% for all the studied metal) prevailed at pH values (ranging from 5.9 to 7.9) measured during batch experiments.

3.3.1. $2Na^+ \rightarrow Me^{2+}$ exchange isotherms

On the basis of the considerations exposed in section 3.2, it could be ascertained that the ion-exchange between divalent metal ions ($Me^{2+} = Cd^{2+}$, Fe^{2+}, Ni^{2+} or Pb^{2+}) in solution and Na^+ ions associated with the brick took place according to the *general* chemical reaction:

$$2\,(Na^+)_z + (Me^{2+})_s \rightarrow (Me)_z + 2\,(Na^+)_s \qquad (3);$$

where the symbols “s” and “z” refer to the solution phase and zeolite phase, respectively. In order to obtain the ion-exchange isotherm representative of Eq.(3), the ionic equivalent fraction of cationic metal exchanged at the brick surface, denoted $(X_{Me})_z$, was plotted against its ionic equivalent fraction in solution, denoted $(X_{Me})_s$. The equivalent ionic fraction of Me^{2+} (or Na^+) ions in the solid phase was calculated from the equation:

$$(X_{Me})_z = \frac{ionic \cdot equivalent \cdot of \cdot Me^{2+}(or \cdot Na^+) \cdot in \cdot brick}{total \cdot ionic \cdot equivalent \cdot (Me^{2+} + Na^+) \cdot in \cdot brick} \quad (4)$$

The equivalent ionic fraction of Me^{2+} (or Na^+) ions in the liquid phase is defined as the ratio of the normality of Me^{2+} (or Na^+) to the total normality (Me^{2+} + Na^+) in the aqueous phase:

$$(X_{Me})_s = \frac{ionic \cdot equivalent \cdot of \cdot Me^{2+}(or \cdot Na^+) \cdot in \cdot solution}{total \cdot ionic \cdot equivalent \cdot (Me^{2+} + Na^+) \cdot in \cdot solution} \quad (5)$$

The ion-exchange isotherms of cationic metals (Cd^{2+}, Fe^{2+}, Ni^{2+} and Pb^{2+}) in brick suspensions are represented in Fig. 8. As seen in this figure, except partly for nickel(II), all the ionic exchange isotherm curves are well above the diagonal of the diagram, indicating that the treated brick is selective for these cations [53, 54]. Note further that for the nearly entire range of $(X_{Me})_z$ the isotherms remained above the diagonal of the diagram and with no inflection(s) in the isotherms, suggesting that only one site group should intervene in the ion-exchange process [54].

Besides, the obtained ion-exchange isotherms have similar shapes and exhibit a steeper increase in the initial stage, $(X_{Me})s < 0.1$, and then the isotherms increased more gently. The observed shapes are characteristic of a favourable cation-exchange process. For the particular $2Na^+/Pb^{2+}$ exchange process, its isotherm proceeds more steeply than for Cd^{2+}, Fe^{2+} and Ni^{2+}. Thus, in the initial stage of the equivalent ion fraction in the solution, $(X_{Me})_s = 0.1$, the isotherm proceeds steeply up to $(X_{Me})_z \approx 0.80$ for lead(II), ≈ 0.68 for cadmium(II), ≈ 0.58 for iron(II) and ≈ 0.40 for nickel(II) (Fig. 8). This observation suggested a higher selectivity of the brick for lead(II) than for cadmium(II), followed by iron(II) and nickel(II).

One could then conclude that from isotherms analysis the brick selectivity for metals increased in the following order: Ni < Fe < Cd < Pb.

3.3.2. Competitive ion-exchanges in binary metals systems

In order to evaluate the mutual effects of the following coexisting heavy metals: Pb(II) - Cd(II), Pb(II) - Ni(II) and Cd(II) – Ni(II) on their respective exchange at the brick-water interface, we carried out at room temperature a series of tests concerning $2Na^{+}\rightarrow Me^{2+}$ exchanges by varying initial metal concentration in solution from 0 to about 10 mmolL^{-1} (Fig. 9). At the equilibrium state, the amount of exchanged metal, Q_e (mmolg^{-1}) was plotted against the metal concentration in solution, C_e (mmolL^{-1}). As a whole, it was noticed two features: (i) except for lead(II), the exchange capacities of studied divalent metals by the brick in binary-metals systems at different initial concentrations were lower than those found in single-metal systems; and (ii) the gap in exchange capacity between them increased with an increase of their initial concentration. In what follows, some additional and relevant remarks were made about the different binary-metals systems studied.

For the Pb(II) - Cd(II) system , the exchange of Pb^{2+} ions in solution by Na^{+} ions associated with the brick was affected weakly and even enhanced in comparison with that obtained in the single-metal system (Fig. 9a). Indeed, the exchange capacity of Pb(II) at different initial concentrations almost maintained at the same level and, in some experiments, was found to be slightly higher as that in case no Cd(II) was added in the medium. Conversely, the Cd(II) exchange on the brick was strongly inhibited in the presence of lead(II) (Fig. 9a). Thus, the exchange capacity for Cd(II) in single-metal system at the equilibrium metal concentration of ≈1.0 mmolL^{-1} was about 0.07 mmolg^{-1}, while it dropped to 0.046 mmolg^{-1} in binary-metals system. This difference suggested that a competitive ion-exchange took place when Pb(II) and Cd(II) coexisted in the aqueous phase. Therefore, treated brick was more favourable to exchange its surface Na with Pb^{2+} ions than with Cd^{2+}, especially when there were insufficient (active) brick sites. Hence, in binary-metals system with high initial concentrations of Pb and Cd, the available brick sites were occupied more preferentially by lead(II).

For the Pb(II) - Ni(II) system , the exchange of Pb^{2+} ions in solution by Na^{+} ions bound to the brick was weakly affected in comparison with that observed in the single-metal system (Fig. 9b). Conversely, the Ni(II) exchange on the brick was more strongly inhibited in the presence of lead(II) than that observed for Cd(II) in the Pb(II)-Cd(II) system (Fig. 9b). These observations confirmed that the available brick sites were occupied almost essentially by lead(II) at the expense of Ni^{2+} ions, even at low initial concentrations of metal ions.

For the Cd(II) - Ni(II) system , the exchanges of both Ni^{2+} ions and Cd^{2+} ions in solution by Na^{+} ions bound to the brick were highly affected when compared to the curves obtained with single-metal systems (Fig. 9c). Therefore, cadmium and nickel were competed strongly each other, nevertheless, with a better affinity of the brick towards cadmium.

In order to confirm the obtained selectivity sequence, we afterwards examined the mutual effects of a mixture of Pb^{2+}, Cd^{2+} and Ni^{2+} ions (in a tertiary system) on their respective exchange at the brick-water interface according the same procedure described above for binary systems. As seen in Fig. 9d, the brick showed the highest exchange capacity toward lead(II), followed by cadmium(II) and nickel(II), which was consistent with findings on binary-systems. In addition, the exchange of Pb^{2+} ions in solution by Na^{+} ions bound to the brick was weakly affected, confirming that the available brick sites were preferentially occupied by lead(II).

By applying the Langmuir isotherm model to binary-metals systems, it was previously demonstrated that the simulation results closely matched with experimental ones [46]. High correlation coefficients ($R^2 > 0.99$) were obtained, indicating that the competitive Langmuir isotherm model could describe accurately the ion-exchange behaviour of Cd(II), Ni(II) and

Pb(II) on brick surfaces in binary-metals systems. This model was thereby employed to predict the ion-exchange capacities of divalent metals in binary-metals system by modified brick. Thus, in the binary Pb(II)-Cd(II) system the maximum ion-exchange amount of Pb(II) (Q_{max} = 0.222 mmolg^{-1}) decreased more slightly than that of Cd(II) (Q_{max} = 0.099 mmolg^{-1}) when compared to Langmuir model data in single metal system (Q_{max}(single) = 0.366 and 0.255 mmolg^{-1} for Pb^{2+} and Cd^{2+}, respectively). In the binary Pb(II)-Ni(II) system, the maximum ion-exchange amount of Pb(II) (Q_{max} = 0.406 mmolg^{-1}) was enhanced, while that of Ni(II) decreased significantly (Q_{max} = 0.049 mmolg^{-1}) when compared to Langmuir model results in single-nickel system: Q_{max}(single) = 0.179 mmolg^{-1}). In the binary Cd(II)-Ni(II) system, the maximum ion-exchange amount of Cd(II) (Q_{max} = 0.108 mmolg^{-1}) decreased as that of Ni(II) (Q_{max} = 0.048 mmolg^{-1}). As for the Pb(II)- Cd(II-Ni(II) tertiary system, the findings did confirm the preference of active brick sites for lead(II) following by cadmium(II) and nickel(II).

In the following paragraph, we addressed some thermodynamic aspects of $2Na^+ \rightarrow Me^{2+}$ and $Me_1{}^{2+} \rightarrow Me_2{}^{2+}$ exchanges (with Me = Cd, Ni, Fe and Pb) at the brick-water interface.

3.4. Thermodynamic approach of ion-exchanges on alkali brick

3.4.1. $2Na^+ \rightarrow Me^{2+}$ exchanges (Kielland plots)

Following a thermodynamic model in which brick zeolites have an ideal behaviour, the thermodynamic equilibrium constant for ion-exchange process (3) denoted the Kielland quotient (K_c), can be determined from the equation:

$$K_c = \frac{(X_{Me})_z . a^2_{Na+} . f_{Me\,2+}}{(X_{Na})^2_z . a_{Me\,2+} . f^2_{Na+}} \quad (6),$$

where a_{Na+} and a_{Me2+} represent the ionic activities of Na^+ and Me^{2+} in solution, respectively; and f_{Na+} and f_{Me2+} are the activity coefficients of Na^+ and Me^{2+} in the brick phase, respectively. If the zeolitic exchanger is taken as pure Na^+ and Me^{2+} forms, the f_{Na+} and f_{Me2+} coefficients could be fixed as unity. As for the ionic activities, a_{Na+} and a_{Me2+}, they were defined as: $a_{Na+} = [Na^+]. \gamma_{Na+}$ and $a_{Me2+} = [Me^{2+}]. \gamma_{Me2+}$, where = $[Na^+]$ and $[Me^{2+}]$ represent the concentration of Na^+ and Me^{2+} in solution; and γ_{Na+} and γ_{Me2+} are the activity coefficients of Na^+ and Me^{2+} in the solution phase, respectively. Activity coefficients were calculated from Debye-Huckel equation [55].

By considering brick−cationic metal combination as solid solution, the thermodynamic equilibrium constant, K_a, for heterogeneous reaction (3) can be calculated by expressing it in terms of ln(Kc), as[56, 57]:

$$\ln K_a = (Z_{Na+} - Z_{Me\,2+}) + \int_0^1 \ln K_c.d(X_{Me})_z \qquad (7);$$

where Z_{Na+} and Z_{Me2+} represent the charge of Na^+ and Me^{2+}, respectively. The logarithm of K_c was plotted against the equivalent ionic fraction of cationic metal in the brick, $(X_{Me})_z$. The obtained curve is termed the *Kielland plot* (see Fig. 10). This plot was employed for assessing the integral of Eq.(7). Using the Excel program, the integral term on the right-hand side of Eq. (7) was evaluated by integrating the best-fit polynomial of the experimental plot of $\ln(K_c)$ *versus* $(X_{Me})_z$ shown in Fig. 10. The polynomial expression for lnKc (see Eq.8) was determined for the different $2Na^+ \rightarrow Me^{2+}$ exchange reactions and listed in Table 1.

$$\ln Kc = C_0 + C_1(X_{Me})_z^1 + C_2(X_{Me})_z^2 + C_3(X_{Me})_z^3 + C_4(X_{Me})_z^4 \qquad (8)$$

The resulting $\ln K_a$ values are given in Table 2. As seen in this table, thermodynamic calculations indicated the following selectivity sequence: $Pb^{2+} > Cd^{2+} > Fe^{2+} > Ni^{2+}$. This order was the same as that obtained with ion-exchange isotherms (see section 3.3). It was further interesting to note that the obtained selectivity sequence was comparable to those reported in the literature for LTA zeolite (Si/Al ratio = 1) [58]. In Table 2, we also reported the $\ln K_a$ constants found for some other zeolites with low Si/Al ratios such as: phillipsites

(Si/Al = 2.47); chabazites (Si/Al = 2.44-2.54); and clinoptilolites (Si/Al = 4.17) [59]. These $\ln K_a$ values differed from those obtained in this work due to the different Si/Al ratios and crystalline nature of natural zeolites (chabazites, clinoptilolites and phillipsites) when compared to zeolites NaA and NaP present in the alkali brick.

The standard free energy per equivalent of exchange ions, $\Delta G_a°$, was calculated from the equation [60, 61]:

$$\Delta G_a^o = \frac{-RT}{z_{Na+} \cdot z_{Me2+}} \ln K_a \qquad (9)$$

The obtained values are listed in Table 2. It can be noticed that the $\Delta G_a°$ value for the $2Na^+ \rightarrow Pb^{2+}$ exchange is the smallest value, while that for the $2Na^+ \rightarrow Ni^{2+}$ exchange is the highest one. Based on standard Gibbs energy, the selectivity follows the order: $Pb^{2+} > Cd^{2+} > Fe^{2+} > Ni^{2+}$, which is in accordance with that found above from isotherms data. Note also that the $\Delta G_a°$ values for the $2Na^+ \rightarrow Me^{2+}$ exchanges (with $Me^{2+} = Cd^{2+}$, Ni^{2+} and Pb^{2+}) on alkali brick are similar enough to those obtained previously on LTA [58].

3.4.2. $Me1^{2+} \rightarrow Me2^{2+}$ exchanges

The thermodynamic equilibrium constant for heterogeneous reaction (10), $\ln K_a^*$, was assessed as a means to describe the selectivity/un-selectivity of the modified brick for a given couple such as: Ni-Cd, Ni-Fe, Ni-Pb or Cd-Pb.

$$2\,(Me1^{2+})_z + (Me2^{2+})_s \rightarrow (Me2)_z + 2\,(Me1^{2+})_s \qquad (10)$$

The equilibrium constant for reaction (10) can be calculated from the expression:

$$K_a^* = \frac{K_a(2Na^+ \rightarrow Me2^{2+})}{K_a(2Na^+ \rightarrow Me1^{2+})} \qquad (11)$$

Table 3 reports the values of the equilibrium constants ($\ln K_a^*$) and the corresponding variation of free energy (ΔG_a^*) for different couples of studied divalent metals (***i.e.***, Cd^{2+}, Fe^{2+}, Ni^{2+} and Pb^{2+}).

It could be noticed that the magnitude of the $\ln K_a^*$ values obtained for the couples Cd-Pb, Ni-Pb and Ni-Cd confirmed relatively well the observations made during batch experiments about the competitive interactions of $Cd^{2+} + Pb^{2+}$, $Ni^{2+} + Pb^{2+}$ and $Ni^{2+} + Cd^{2+}$ mixtures with alkali brick in water. (See section 3.3.2).

3.5. Determining factors for ion-exchange of heavy metal ions on alkali brick

Thermodynamic equilibrium constants for the exchange reactions: $2Na^+ \rightarrow Me^{2+}$ and $Me_1^{2+} \rightarrow Me_2^{2+}$ both followed the affinity sequence: $Ni^{2+} < Fe^{2+} < Cd^{2+} < Pb^{2+}$. This order is partially comparable with that found for instances: by Choi and his co-workers [64] ($Cd^{2+} < Pb^{2+}$) when using Mg-modified zeolite as adsorbent; and by Ezzeddine and his co-workers [58] ($Ni^{2+} < Cd^{2+} < Pb^{2+}$) when using NaX and LTA zeolites. However, the obtained affinity sequence ($Ni^{2+} < Fe^{2+} < Cd^{2+} < Pb^{2+}$) differs somewhat from that found for instance by Visa [65] and Qiu and his co-workers [66], ***i.e.***: $Cd^{2+} < Ni^{2+} < Pb^{2+}$ when using zeolite materials derived from fly ashes. In previous works [66- 70], the authors ascertained that the observed differences in adsorption performance of zeolitic materials toward heavy metal cations were related not only to the cations physico-chemistry in water, but also to the crystalline/textural/morphological properties of zeolitic frameworks and their pore size distribution. Indeed, hydrated metal ions had to move through the zeolitic pores and channels of the lattice by diffusion, leading to the replacement of the exchangeable cation, Na^+.

In what follows, some attempts were made to examine and analyse qualitatively the relative tendency of cationic metal to exchange with Na^+ ions at brick surfaces from aqueous solutions by trying to find specific correlations: *first* between some thermodynamic and physico-chemical parameters of metal ions and thermodynamic equilibrium constants for $2Na^{+} \rightarrow Me^{2+}$ exchange; and *second* between framework/porosity characteristics of modified brick and K_a constants.

3.5.1. Implication of cationic-metal behaviour on ion-exchange

*Heavy metal radius*__ According to Marcus'works [71], divalent metal with an ionic radius, R_i is surrounded in water by a spherical shell, ΔR_{H2O}, in which several H_20 molecules are immobilized by the electrostatic field of the cationic metal. The total distance from the center of the metal ion till the edge of the shell is then given by: $R_{Total} = R_i + \Delta R_{H2O}$. The values of R_{Total} (R_H = hydrated radius), R_i, and ΔR_{H2O} for Cd^{2+}, Fe^{2+}, Ni^{2+} and Pb^{2+} ions are listed in Table 4. Fig. 11a displays the change in hydrated radius ($R_{H.}$) in relation to the thermodynamic equilibrium constant (lnK_a) for the $2Na^{+} \rightarrow Me^{2+}$ exchange on brick-derived zeolites. As can be seen in this figure, the logarithm of the K_a constant exhibits a good correlation with hydrated radius (with a correlation coefficient, R^2 equal to 0.9904). This R_H dependence on the lnK_a value can be explained by the fact that, when the medium pH is above the pH at the point of zero charge of the brick, a low cation size allows better Coulombic attractions of ionic species in solution towards negatively charged brick surfaces. Similar trends were observed in previous works, for instances, about the adsorbent properties of certain soils: indeed these researches revealed that the Pb^{2+} entity was preferably adsorbed on to these soils as compared to Ni^{2+}, Zn^{2+} and Mn^{2+} [72] and to Cd^{2+} [73].

*Ionic potential*__ This parameter is an indicator of the electrostatic properties of an ion when interacting with other ions either of similar charge (yielding electrostatic repulsion forces) or of opposite charge (yielding electrostatic attraction forces). Ionic potential is the ratio of the electrical charge of an ion (*Z*) to its radius (*R*). It was previously considered as an important criterion for the choice of efficient adsorbents for toxic elements [74]. In order to calculate the ionic potential, we fixed Z = +2 for cationic metals and took the hydrated radius of the metal ion (R_H) which was estimated from Marcus's works [71]. The Z/R_H values are listed in Table 4. Fig. 11b shows the evolution of the equilibrium constant, $\ln K_a$, as a function of the ratio Z/R_H. The $\ln K_a$ constant exhibits a good correlation with the ratio Z/R_H (the correlation coefficient, R^2, is equal to 0.9915). The obtained profile seems to suggest a noticeable contribution of electrostatic forces to the ion-exchange mechanism.

*Hydration free energy*__ An interpretation of thermodynamic data was attempted to be made in the light of the Eisenman-Sherry theory of cation exchange selectivity in zeolites [75, 76]. According this theory, the behaviour of zeolites towards competing cations should depend markedly on the cation free energy of hydration. On this basis, we decided to examine the contribution of hydration free energy of each metal ion (Me^{2+}) to the thermodynamic characteristics of the $2Na^+ \rightarrow Me^{2+}$ exchange reaction occurring at the brick-water interface.. The association between a heavy metal cation and water molecules leads to the formation of a hydration shell and the release of (exothermic) hydration free energy, "ΔG_H". Fig. 11c compares the thermodynamic equilibrium constant, $\ln K_a$, for each selected divalent metal to its free energy of hydration, $\Delta G_{H.}$. For that, we used the values of "ΔG_H" reported recently by Kepp [77] (see also Table 5). As seen in Fig.11c, the $\ln K_a$ constant exhibits a relatively good correlation with hydration free energy (with a correlation coefficient, R^2, equal to 0.9064). Metal cations with smaller "exothermic" hydration free energy like Pb^{2+} and Cd^{2+} ions [-1513 $kJmol^{-1}$ for Pb(II) and -1843 $kJmol^{-1}$ for Cd(II)], have softer hydration shells than Fe^{2+} ion (-1928 $kJmol^{-1}$), or Ni^{2+} ion (-2068 $kJmol^{-1}$). Hence, when cations bind to active brick sites the thermodynamic behaviour of hydrated lead(II) and cadmium(II) in water enabled an easier rearrangement and loss of the water molecules of hydration around positively charged ions than for hydrated iron(II) and nickel(II) (before diffusing inside zeolitic pores/channels). Concerning the sequence of selectivity of the brick for heavy metals, Pb(II) possessed the higher free energy of hydration (-1513 kJmol^{-1} [77]) followed by Cd(II) (-1843 kJmol^{-1} [77]), Fe(II) (-1928 kJmol^{-1} [77]) and Ni(II) (-2068 kJmol^{-1} [77]). This observation was therefore well in accordance with the Eisenman-Sherry theory. Note further that the order of metal selectivity agreed well with those of solvation ($\Delta G_{solv,\ Me2+}$) and non-solvation ($\Delta G_{n,Me2+}$) energies (see Table 5), thus evidencing the importance of (intrinsic) physico-chemical and thermodynamic properties of the metal ion in water on the course of the heterogeneous process.

3.5.2. Effects of brick characteristics on ion exchange

Previously, the ability of the brick treated with sodium hydroxide to uptake cationic metals was examined kinetically and results revealed that the process was rapid, even by stirring very gingerly (or not) suspensions (within the first 20 min of contact at 298 K, more than 70% of metal ions in the solution were exchanged with brick sodium and saturation was reached after about 250 min) [45]. Kinetic data were well explained by applying both the pseudo-second-order rate model and Weber-Morris intra-particle diffusion model. This latter model proved that two steps (film diffusion and diffusion within porous brick zeolites) controlled the metal-uptake process [45].

Besides, it is worth to note that the raw brick was preliminarily tested as an ion exchanger for heavy metal cations, and data revealed a very low uptake process [51]. This suggested that, after brick zeolitization, the other (un-reacted) crystals / porous structures present in the raw brick (quartz, illite and rutile, see Fig. 2A) do not (or barely) affect the ion exchange of metal ions on generated zeolites.

*Kinetic aspects*__ The pseudo second-order rate constants (k_2) for the removals of metal cations ((Cd^{2+}, Fe^{2+}, Ni^{2+} and Pb^{2+})) by alkali brick from aqueous solutions are listed in Table 5). In the present work, we plotted the thermodynamic equilibrium constant for

$2Na^{+}\rightarrow Me^{2+}$ exchange ($\ln K_a$) against the pseudo-second-order rate constant (k_2) and found a relatively good correlation between $\ln K_a$ and k_2 ($R^2 = 0.9509$; as shown in Fig. 11d). This correlation revealed two features: (i) a significant influence of the reaction kinetics on the ion-exchange equilibrium; and (ii) an ion-exchange performance of the brick towards heavy metals which seems to be intimately related to the kinetics order: $Pb^{2+} > Cd^{2+} > Fe^{2+} > Ni^{2+}$.

On the other hand, in a recent article [45] we reported that early-stage kinetic data were fitted well with the following early-stage kinetic equation: $Q_t = r_o.t/(1 + a.t)$ (where "Q_t" represents the amount of metal bound to the brick; and "r_o" and "a" are fitting parameters); And owing to this equation we determined the initial adsorption rate (r_o) by linear regression (the r_o values are listed in Table 4). In the present work, we plotted the obtained thermodynamic equilibrium constant ($\ln K_a$) against the initial adsorption rate (r_o) which was previously estimated for $2Na^{+} \rightarrow Me^{2+}$ exchanges on alkali brick [45]. As seen in Fig. 12a, the $\ln K_a$ constant displays a relatively good correlation with the r_o rate ($R^2 = 0.9982$). Furthermore, this correlation between the thermodynamic behaviour of $2Na^{+}\rightarrow Me^{2+}$ exchange and its early-stage kinetics indicated again a better affinity of the brick toward lead(II) than toward cadmium(II), and (in a decreasing order) toward iron(II) and nickel(II).

To summarize, the above observations would suggest the implication of kinetic characteristics on the thermodynamics of $2Na^{+}\rightarrow Me^{2+}$ exchanges on alkali brick. Unfortunately, classical pseudo-second-order kinetic models permitted to examine only the whole $2Na^{+}\rightarrow Me^{2+}$ exchange/adsorption process but, they did not take into consideration the involvement of surface mechanistic steps ***i.e.***: film mass transfer and surface diffusion through porous materials like zeolitic frameworks.

Consequently, to better appraise the contribution of kinetic effects on the thermodynamics of the ion-exchange process, it was necessary to take into consideration the porous nature of the modified brick. As meso-pores on brick-derived zeolites are as major active sites, the pore size should play an important role in the metal capacity of the brick. On this view, diffusion-based models which were frequently applied in the past to porous materials [79-82] would represent more realistically the kinetics for alkali brick. Recently, we attempted to apply diffusional mass transfer models to our system and, the obtained results revealed that the kinetics of the ion-exchange process at the brick surface was occurred according three successive steps: external mass transfer; intra-particle diffusion; and adsorption on active brick sites [45].

In the assumption that a smaller cation might pass through the pores/channels of the zeolite structure with ease, a relationship between the magnitude of metal uptake and the contribution of surface diffusion should then exist. To check this, a correlation analysis between thermodynamic properties and mass transfer/diffusion parameters obtained for $2Na^{+} \rightarrow Me^{2+}$ exchanges was undertaken in the following section.

*Mass transfer / surface diffusion effects*__ In recent works [45], we applied to $2Na^{+} \rightarrow Me^{2+}$ exchanges onto alkali brick a simplified method developed by Yao and Chen [79] for evaluating parameters relative to film mass transfer and surface diffusion phenomena from batch kinetic data. Yao and Chen [79] showed also that the surface diffusion coefficient depended upon the late-stage adsorption rate constant (k_e). On this basis, we further calculated the k_e value for each studied metal cation by regression of the late-stage kinetic data and these findings were recently published [45]. In the present work, we plotted the obtained thermodynamic equilibrium constant ($\ln K_a$) against the rate constant k_e (Table 4). As seen in Fig. 12b, the $\ln K_a$ constant exhibits a relatively good correlation with the rate constant k_e ($R^2 = 0.9501$), indicating a contribution of surface-diffusion phenomena to the thermodynamics of ion-exchange reactions at brick surfaces.

Moreover, in Fig. 12c we plotted the thermodynamic equilibrium constant ($\ln K_a$) for the $2Na^+ \rightarrow Me^{2+}$ exchange against the diffusion coefficient (both the film diffusion coefficient, D_1, and pore diffusion coefficient, D_2; see Table 4). As seen in this figure, the $\ln K_a$ constant tends roughly to increase with the magnitude of the metal diffusion, indicating that, when metal ions diffuse more easily through pores/channels of brick zeolites, the diffusion phenomenon contributes to favour the ion-exchange reaction as well. Similar findings were obtained when plotting the $\ln K_a$ constant against the surface diffusion coefficient, Ds (see Fig. 12d). The Ds values were previously calculated [45] by using the Yao-Chen simplified method [79] (see Table 4).

Overall, the above results indicated that the ion-exchange process was significantly affected by mass transfer/diffusion due to the pore structures of brick-derived zeolites. The rates of diffusion and the thermodynamic constants (K_a) were in the order: $Pb^{2+} > Cd^{2+} > Fe^{2+} > Ni^{2+}$; this sequence was in agreement with the fact that the smallest cations (Pb^{2+}) was ideally be exchanged faster and in larger quantities compared to the larger cations. In other words, a more favourable diffusion of ions through zeolitic networks contributed to an increase in the exothermy of the exchange reaction.

Note that machine learning algorithm (Boruta algorithm embedded in R project) was recently employed to rank the importance of the parameters (total energy, pore size, and average volume) on the loading capacity of heavy metals on the zeolitic framework [83]. By employing molecular simulations, computational approach could adequately justify the ion-exchange performance differences of heavy metals by zeolites, observing particularly the following frequent trend: $Pb^{2+} > Cd^{2+} > Ni^{2+}$, which agreed well with our findings.

.4. Conclusions

After chemical and structural modifications of a brick derived from Bangui soils, the potential uses of this modified brick (in Na-forms) were evaluated as an adsorbent for heavy metals decontamination of wastewaters. XRD and ESEM/EDS analyses revealed the generation of sodic zeolites (NaA and NaP) through the hydroxylation of metakaolinite present in the raw brick by sodium hydroxide. Porosity studies showed the mesoporous characteristics of the brick, and particularly, an increase of smaller mesopores (diameters: 37-40 Å) after its zeolitization.

In single-metal systems, the ion-exchange isotherms relative to the different reactions between treated brick and divalent metal cations (Cd^{2+}, Fe^{2+}, Ni^{2+} and Pb^{2+}) revealed favourable heterogeneous processes with a higher selectivity for lead than the other three metals. Kielland quotients were determined for the different studied ion exchanges and permitted to estimate corresponding thermodynamic equilibrium constants by using Gaines - Thomas expression. Based on these results, the brick selectivity followed the order: Pb > Cd > Fe > Ni. Hydrated radius, ionic potential and hydration free energy were found to be relatively well correlated with the thermodynamic equilibrium constant (K_a) for the $2Na^+ \rightarrow Me^{2+}$ heterogeneous reaction, confirming the implication of physico-chemical and thermodynamic properties of hydrated cationic metals on the thermodynamics of the ion-exchange/adsorption mechanism. However, a satisfying response for understanding metal affinity and selectivity could not be made adequately without further taking into consideration the structural / morphological / electro-kinetic characteristics of the brick and its porosity in the ion-exchange mechanism. Kinetic rates and mass-transfer and diffusion parameters were found to be as well good indicators of the thermodynamic behaviour of the studied process in which: (i) preliminarily, hydrated metal cation would lose water molecules from its hydration shell when the ionic species attained the brick surface; and (ii) subsequently, resulting cation dehydration would facilitate the transfer and diffusion of metal through pores/channels of brick-derived zeolites (NaA and NaP).

CRedit author statement

Oscar Allahdin: Conceptualization, Methodology, Software, Validation, Formal analysis. **Nicole Poumaye:** Conceptualization, Methodology, Software, Validation, Formal analysis. **Michel Wartel:** Conceptualization, Methodology, Supervision. **Abdel Boughriet:** Conceptualization, Methodology, Writing.

Declaration of Competing Interest

The authors declare no competing financial interests.

Acknowledgments

These scientific works were undertaken successfully owing to the cooperation between the University of Lille (France) and the University of Bangui (Central African Republic). This collaboration (being still under way) and the Grant-in-Aid to Nicole Poumaye for her Doctoral-Thesis preparation have been financially supported by the Embassy of France at Bangui. The authors gratefully thank David Dumoulin (Chemical Engineer) and Véronique Alaimo (Chemical Technicians) for helping us usefully in certain delicate chemical and analytical/spectroscopic analyzes, and Laurence Burylo for X-ray diffraction analyzes.

References

[1] N. Poumaye, O. Allahdin, M. Wartel, A. Boughriet, Hazardous Iron in Contaminated Ground Water (A Special Focus in Central African Republic): Health Risk Assessment and

Efficient Ferrous Ions Removal by Activated Brick. International Journal of Pharmacy & Pharmaceutical Research 16(3) (2019) 288-305.

[2] World Health Organization, Guidelines for Drinking Water Quality, recommendations, Vol. 1, WHO, Geneva, Switzerland, 1984, p. 79.

[3] S. Chaturvedi, P.N. Dave, Removal of iron for safe drinking water, Desalination 303 (2012) 1-11.

[4] N. Khatri, S. Tyagi, D. Rawtani, Recent Strategies for the removal of iron from water: A review, Journal of Water Process Engineering 19 (2017) 291-304.

[5] G.D. Michalakos, J.M. Nieva, D.V. Vayenas, G. Lyberatos, Removal of iron from potable water using a Trickling filter, Wat. Res. 31(5) (1997) 991–996.

[6] P. Colvin, V. Filipova, A. Masic, Iron Removal.VVAN01 Decentralized Water and Wastewater Treatment, (2017) www.chemeng.lth.se/vvan01/Arkiv/ExerciseB_Ironremoval.pdf2011

[7] Tech Brief: Iron and Manganese Removal, A National Drinking water Clearinghouse Fact Sheet, NINE- September 1998, item #DWBLPE70, 1998, pp. 1-4.

[8] J. Hartmann, F. Braulke, U. Sinzig, G. Wulf, J.H. Maas, F. Konietschke, D. Haase, Iron overload impairs proliferation of erythroid progenitors cells (BFU-E) from patients with myelodysplastic syndromes, Leuk. Res. 37 (2013) 327–332.

[9] X. Chai, D. Li, X. Cao, Y. Zhang, J. Mu, W. Lu, X. Xiao, C. Li, J. Meng, J. Chen, Q. Li, J. Wang, A. Meng, M. Zhao, ROS-mediated iron overload injures the hematopoiesis of bone marrow by damaging hematopoietic stem/progenitor cells in mice, Sci. Rep. 5 (2015) 10181.

[10] Y.Y. Jang, S.J. Sharkis, A low level of reactive oxygen species selects for primitive hematopoietic stem cells that may reside in the low-oxygenic niche. Blood 110 (2007) 3056–3063.

[11] L. Shao, H. Li, S.K. Pazhanisamy, A. Meng, Y. Wang, D. Zhou, Reactive oxygen species and hematopoietic stem cell senescence. Int. J. Hematol. 94 (2011) 24–32.

[12] C. Frippiat, J. Dewelle, J. Remacle, O. Toussaint, Signal transduction in H_2O_2 induced senescence - like phenotype in human diploid fibroblasts, Free Radic. Biol. Med. 33 (2002) 1334–1346.

[13] E. Prus, E. Fibach, Effect of iron chelators on labile iron and oxidative status of thalassaemic erythroid cells, Acta Haematol. 123 (2010) 14–20.

[14] World Health Organization (WHO). Iron in Drinking-water. In: WHO Guidelines for drinking-water quality, 2nd ed. Vol. 2. Health criteria and other supporting information. World Health Organization, Geneva, 1996.

[15] V.K. Gupta, P.J.M. Carrott, P.J.M., M.L. Ribeiro, Carrott, Dr. Suhas, Low-cost adsorbents: growing approach to wastewater treatment -a review, Critical Reviews in Environmental Science and Technology 39 (10) (2009) 783-842. https://doi.org/10.1080/10643380801977610

[16] J. Peng, Y. Song, P. Yuan, X. Cui, G. Qiu, G., The remediation of heavy metals contaminated sediment. J. Hazard Mater. 161 (2009) 633-640.

[17] M.I. Inyang, B. Gao, Y. Yao, Y. Xue, A. Zimmerman, A. Mosa, P. Pullammanappallil, Y.S. Ok, X. Cao, A review of biochar as a low-cost adsorbent for aqueous heavy metal removal. Crit. Rev. Environ. Sci. Technol. 46 (2016) 406-433.

[18] E. A. Al-Abbad, R. A. Al Dwairi, Removal of nickel (II) ions from water by Jordan natural zeolite as sorbent material, Journal of Saudi Chemical Society 25 (2021) 101233, 1-10. https://doi.org/10.1016/j.jscs.2021.101233

[19] L. Sellaoui, E. P. Hessou, M. Badawi, M. S. Netto, G. L. Dotto, L. F. Oliveira Silva, F. Tielens, J. Ifthikar, A. Bonilla-Petriciolet, Z. Chen, Trapping of Ag+, Cu2+, and Co2+ by faujasite zeolite Y: New interpretations of the adsorption mechanism via DFT and statistical modeling investigation, Chemical Engineering Journal 420 (2021) 127712, 1-9. https://doi.org/10.1016/j.cej.2020.127712

[20] A. Khalil, R. Hashaikeh, N. Hilal, 3D printed zeolite-Y for removing heavy metals from water, Journal of Water Process Engineering 42 (2021) 102187, 1-11. https://doi.org/10.1016/j.jwpe.2021.102187

[21] Y. Kobayashi, F. Ogata, T. Nakamura, N. Kawasaki, Synthesis of novel zeolites produced from fly ash by hydrothermal treatment in alkaline solution and its evaluation as an adsorbent for heavy metal removal, Journal of Environmental Chemical Engineering 8 (2020) 103687, 1-6. https://doi.org/10.1016/j.jece.2020.103687

[22] R. Zheng, X. Feng, W. Zou, R. Wang, D. Yang, W. Wei, S. Li, H. Chen, Converting loess into zeolite for heavy metal polluted soil remediation based on "soil for soil-remediation" strategy, Journal of Hazardous Materials 412 (2021) 125199, 1-9. https://doi.org/10.1016/j.jhazmat.2021.125199

[23] L. Roshanfekr Rad, M. Anbia, Zeolite-based composites for the adsorption of toxic matters from water: A review, Journal of Environmental Chemical Engineering 9 (2021) 106088, 1-22. https://doi.org/10.1016/j.jece.2021.106088

[24] N.S. Labidi, Removal of mercury from aqueous solutions by waste brick. Inter. J. Environ. Res. 2(3) (2008) 275-278.

[25] A. Witharana, M. Jayaweera, J. Manatunge, Zinc adsorption by low cost sorbent materials: Clay title, brick, sawdust and rice husk. International Conference on Sustainable Built Environment (ICSBE-2010), Kandy, 13-14 Decembre 2010, pp. 21-28.

[26] N. Gandhi, D. Sirisha, K.B. Chandra Sekhar, Adsorption studies of chromium by using low cost adsorbents. Our Nature 11(1) (2013) 11-16.

[27] P.V. Hemalatha, P.V.V. Prasada Rao, Adsorption batch studies on calcined brick powder in removing chromium and nickel ions. Inter. J. Adv. Res. Chem. Sci. 1(6) (2014) 14-21.

[28] R.H. Krishna, AV.V.S. Swamy, Physico-chemical key parameters, Langmuir and Freundlich isotherm and Lagergren rate constant studies on the removal of calcined brick, Inter. J. Eng. Res. Dev. 4(1) (2012) 29-38.

[29] S.C. Dehou, M. Wartel, P. Recourt, B. Revel, J. Mabingui, A. Montiel, A. Boughriet, Physicochemical, crystalline and morphological characteristics of bricks used for ground waters purification in Bangui region (Central African Republic), Appl. Clay Sci. 59-60 (2012) 69-75.

[30] S.C. Dehou, J. Mabingui, L. Lesven, M. Wartel, A. Boughriet, Improvement of Fe(II)-adsorption capacity of FeOOH-coated brick in solutions, and kinetics aspects, J. Water Resourc. Protection 4 (2012) 464-473.

[31] O. Allahdin, S.C. Dehou, M. Wartel, P. Recourt, M. Trentesaux, J. Mabingui, A. Boughriet, Performance of FeOOH-brick based composite for Fe(II) removal from water in fixed bed column and mechanistic aspects, Chem. Eng. Res. and Design 91 (2013) 2732-2742. http://dx.doi.org/10.1016/j.cherd.2013.04.006

[32] O. Allahdin, M. Wartel, P. Recourt, B. Revel, B. Ouddane, G. Billon, J. Mabingui, A. Boughriet, Adsorption capacity of iron oxyhydroxide-coated brick for cationic metals and nature of ion surface interactions, Appl. Clay Sci. 90 (2014) 141–149.

[33] O. Allahdin, M. Wartel, J. Mabingui, A. Boughriet, Kinetics of divalent Metals (Cd^{2+}, Cu^{2+}, Pb^{2+}, Zn^{2+}) adsorption onto a modified brick, Am. Chem. Sci. J., 4(5) (2014) 687-705.

[34] O. Allahdin, M. Wartel, J. Mabingui, A. Boughriet, Implication of electrostatic forces on the adsorption capacity of a modified brick for the removal of divalent cations from water. Am. J. Anal. Chem. 6 (2015) 11-25.

[35] O. Allahdin, B. Bagoua, M. Wartel, J. Mabingui, A. Boughriet, Effects of chemical activation on surface sites of the brick: pH-dependence on metal adsorption, International J. New Technol. Res., 2(1) (2016) 22-31.

[36] J. Temuujin, K. Okada, K.J.D. MacKenzie, Zeolite formation by hydrothermal treatment of waste solution from selectively leached kaolinite, Materials Letters 52 (2002) 91-95.

[37] E.B.G. Johnson, S.E Arshad, Hydrothermally synthesized zeolites based on kaolinite: A review, Applied Clay Science 97-98 (2014) 215-221.

[38] L. Ayele, J. Pérez-Pariente, Y. Chebude, I. Diaz, Synthesis of zeolite A from Ethiopian kaolin. Microporous and Mesoporous Materials 215 (2015) 29-36.

[39] N. Poumaye, O. Allahdin, G. Tricot, B. Revel, G. Billon, P. Recourt, M. Wartel, A. Boughriet, MAS NMR investigations on a metakaolinite-rich brick after zeolitization by alkaline treatments, Microporous and Mesoporous Materials 277 (2019) 1-9.

[40] N.E. Zimmermann, M. Haranczyk, History and utility of zeolite framework-type discovery from a data-science perspective, Cryst. Growth Des. 16 (2016) 3043-3048.

[41] T. Abdullahi, Z. Harun, M.H. Dzarfan Othman, A review on sustainable synthesis of zeolite from kaolinite resources via hydrothermal process, Adv Powder Technol. 28 (2017) 1827-1840.

[42] W. Loewenstein, The distribution of aluminium in the tetrahedral of silicates and aluminates. Am. Mineral. 39 (1954) 92-96.

[43] N. Poumaye, O. Allahdin, M. Wartel, A. Boughriet, Insights into characterization and adsorptive behaviour of zeolitized brick in water toward cadmium (A very toxic heavy metal to humans), Int. J. Pharm. Pharmaceut. Res. 13(3) (2018) 1-29.

[44] N. Poumaye, O. Allahdin, L. Lesven, M. Wartel, A. Boughriet, Adsorption of Iron (II) on Sodic Zeolites─Bearing Brick (In Batch): Insights into Interfacial Chemical Processes and Thermodynamic Equilibria, International Journal of Science and Research Methodology 11(3) (2019) 88-119.

[45] A. Boughriet, N. Poumaye, O. Allahdin, M. Wartel, Kinetic and diffusional aspects of heavy metals adsorption onto zeolitized brick, Advanced Materials and Technologies Environmental Sciences 3(4) (2019) 281-297.

[46] N.M. Poumaye. ***Thesis***: Transformation chimique et Structurale d'un constituant de brique en zéolite: Application à l'élimination des contaminants métalliques dans le traitement des eaux, University of Lille (France), 2020, order number : 109416, pp. 216.

[47] World Health Organization guidelines for drinking water quality. Recommendations, Vol. 1, WHO, 2nd ed. (Geneva), 1993.

[48] L. Heller-Kallai, I. Lapides, Reactions of kaolinites and metakaolinites with NaOH—comparison of different samples (Part 1). Applied Clay Science 35(1-2) (2007) 99-107.

[49] H. Youssef, D. Ibrahim, S. Komarneni. Microwave-assisted versus conventional synthesis of zeolite A from metakaolinite. Microporous and Mesoporous Materials 115 (2008) 527–534. doi:10.1016/j.micromeso.2008.02.030

[50] M.M.J. Treacy, J.B. Higgins. Collection of Simulated XRD Powder Patterns for Zeolites (4th revised Edition), Elsevier, New York, 2001: pp. 174-175 and 212-215.

[51] O. Allahdin. ***Thesis*** : Elimination (par adsorption sur la brique activée) de polluants métalliques dans les eaux de la République Centrafricaine et les pays en voie de développement : Aspects texturaux, physicochimiques, (électro)cinétiques et thermodynamiques. University of Lille (France), 2014, order number: 41530, pp. 177. https://ori.univ-lille1.fr/thematic-search.html?menuKey=these&id=allahdin

[52] A. Boughriet, O? Allahdin, N. Poumaye, M. Wartel, Generation of bridging hydroxyl groups (Si-OH-Al) in synthetic zeolites from brick: (Theoretical) Evidence from electro-kinetic/dielectric/crystallographic properties, and by ^{1}H MAS NMR, *unpublished work.*

[53] G.A. Moamen, H.A. Ibrahim, N. Abdelmonem, I.M Ismail, Thermodynamic analysis for the soptive removal of cesium and strontium ions onto synthesized magnetic nano zeolite, Microporous and Mesoporous Materials 223 (2016) 187-195.

[54] W. Baek, S. Ha, S. Hong, S. Kim, Y. Kim, Cation exchange of cesium and cation selectivity of natural zeolites: Chabazite, stilbite, and heulandite, Microporous and Mesoporous Materials 264 (2018)159-166.

[55] W. Stumm, J.J Morgan, Aquatic Chemistry: Chemical Equilibria and Rates in Natural Waters, Environmental Science and Technology Third edition. John Wiley & Sons, Inc., New York, 1996, pp. 1022.

[56] G.L.Jr. Gaines, H.C. Thomas, Adsorption studies on clay minerals. II. A formulation of the thermodynamics of exchange adsorption: J. Chem. Phys. 21 (1953) 714-718.

[57] D.W. Breck, Zeolite Molecular Sieves: Structure, Chemistry and Use, John Wiley & Sons, New York, 1974, 533-534.

[58] Z. Ezzeddine, I. Batonneau-Gener, Y. Pouilloux, Cation exchange mechanism of divalent metals ions in synthetic NaX and LTA zeolites: Efficiency and selectivity. Eur. Chem. Bull., 2018, 7 (3) (2018) 93-98.

[59] D. Caputo, F. Pepe, Experiments and data processing of ion exchange equilibria involving Italian natural zeolites : a review, Microporous and Mesoporous Materials 105 (2007) 222-231.

[60] R. M. Barrer, S. Barri, J. Klinowski, Zeolite RHO Part 2t.-Cation Exchange Equilibria and Kinetics, J.C.S. Faraday I 76 (1980) 1038-1051.

[61] C. J. Adams, A. Araya, K. J. Cunningham, K. R. Franklin, I. F. White, Measurement and prediction of Ca–Na ion-exchange equilibrium in maximum aluminium P (MAP), a zeolite with the GIS framework topology, J. Chem. Soc., Faraday Trans. 93 (1997) 499-503.

[62] M. Çulfaz,, M. Yagiz, Ion exchange properties of natural clinoptilolite: lead–sodium and cadmium–sodium equilibria, Separation and Purification Technology 37 (2004) 93–105.

[63] I. Rodríguez-Iznaga, G. Rodríguez-Fuentes, V. Petranovskii, Ammonium modified natural clinoptilolite to remove manganese, cobalt and nickel ions from wastewater:

Favorable conditions to the modification and selectivity to the cations, Microporous and Mesoporous Materials 255 (2018) 200-210. http://dx.doi.org/10.1016/j.micromeso.2017.07.034

[64] H.J. Choi, S.W. Yu, K. Han Kim, Efficient use of Mg-modified zeolite in the treatment of aqueous solution contaminated with heavy metal toxic ions, Journal of the Taiwain Institute of Chemical Engineers 63 (2016) 482-489.

[65] M. Visa, Synthesis and characterization of new zeolite materials obtained from fly ash for heavy metals removal in advanced wastewater treatment, Powder Technology 294 (2016) 338–347.

[66] Q Qiu, X. Jiang, G. Lv, Z. Chen, S. Lu, M. Ni, J. Yan, X. Deng, Adsorption of heavy metal ions using zeolite materials of municipal solid waste incineration fly ash modified by microwave-assisted hydrothermal treatment, Powder Technology 335 (2018) 156–163.

[67] E. Erdem, N. Karapinar, R. Donat, The removal of heavy metal cations by natural zeolites, Journal of Colloid and Interface Science 280 (2004) 309–314.

[68] K.S. Hui, Q.Y.H. Chao, S.C. Kot, Removal of mixed heavy metal ions in wastewater by zeolite 4A and residual products from recycled coal fly ash, Journal of Hazardous Materials B127 (2005) 89-101.

[69] V. Frenandez-Montoya, M.A. Pérez-Cruz, D.J. Mendoza-Castillo, M.R. Moreno-Virgen, A. Bonilla-Petriciolet, Competitive adsorption of dyes and heavy metals on zeolitic structures, Journal of Environmental Management 116 (2013) 213-221.

[70] L. Mihaly-Cozmuta, A. Mihaly-Cozmuta, A. Peter, C. Nicula, H. Tutu, D. Silipas, E. Indrea, Adsorption of heavy metal cations by Na-clinoptilolite: Equilibrium and selectivity studies, Journal of Environmental Management 137 (2014) 69-80.

[71] Y. Marcus, A simple empirical model describing the thermodynamics of hydration of ions of widely varying charges, sizes, and shapes, Biophys. Chem. 51 (1994) 111–127.

[72] S. Chotpantarat, S. K. Ong, C. Sutthirat, K. Osathaphan, Competitive sorption and transport of Pb^{2+}, Ni^{2+}, Mn^{2+}, and Zn^{2+} in lateritic soil columns, Journal of Hazardous Materials 190 (2011) 391–396.

[73] J.M. Rodríguez-maroto, R.A. García-delgado, C. Gómez-lahoz, C. Vereda-alonso, F. García-herruzo, M.P.P. Munoz, Competitive retention of lead and cadmium on an agricultural soil, Environ. Monit. Assess. 89 (2003) 165–177.

[74] L. Ronghui; Y. Weiyi; S. Yu; L. Qi; G. Shian; S. Jian Ku, "Ionic potential: A general material criterion for the selection of highly efficient arsenic adsorbents", Journal of Materials Science & Technology 30 (10) (2014) 949–953. *doi:10.1016/j.jmst.2014.08.010. ISSN 1005-0302*.

[75] G. Eisenman, Cation selective glass electrodes and their mode of operation, Biophys. J. 2 (1962) 259- 323.

[76] H.S. Sherry, The ion exchange properties of zeolites. In: J.A. Marinsky (Ed.), Ion Exchange: A Series of Advances, vol. 2. Marcel Dekker, New York, 1969, pp 89–133.

[77] K.P. Kepp, Thermochemically Consistent Free Energies of Hydration for Di- and Trivalent Metal Ions. J. Phys. Chem. A 122 (2018) 7464−7471.

[78] J.C. Torres, J.C. Gubulin, Prediction of ion-interaction parameters of binary 2:1 and 2:2 ion-exchange systems by the coupling of the Margules model with a linear free energy correlation approach, Microporous and Mesoporous Materials 126 (2009) 182-191.

[79] C. Yao, T. Chen, A new simplified method for estimating film mass transfer and surface diffusion coefficients from batch adsorption kinetic data. Chem. Eng. 265 (2015) 93-99.

[80] C. Yao, T Chen, A film-diffusion-based adsorption kinetic equation and its application. Chemical Engineering Research and Design 119 (2017) 87-92.

[81] C. Yao, T. Chen, A weighted average kinetic equation and its application in estimating mass transfer coefficients in liquid phase adsorption. Biophysical Chemistry 211 (2018) 50-54.

[82] V.J. Inglezakis, M.M. Fyrillas J. Park, Variable diffusivity homogeneous surface diffusion model and analysis of merits and fallacies of simplified adsorption kinetics equations. Journal of Hazardous Materials 367 (2019) 224–245. https://doi.org/10.1016/j.jhazmat.2018.12.023

[83] F. S. Wanyonyi, T. T. Fidelis, G. K. Mutua, F. Orata, A. M.S. Pembere, Role of pore chemistry and topology in the heavy metal sorption by zeolites: From molecular simulation to machine learning, Computational Materials Science 195 (2021) 110519, 1-6. https://doi.org/10.1016/j.commatsci.2021.110519

Table captions

Table 1: $2Na^+ \rightarrow Me^{2+}$ exchanges on alkali brick and polynomial expressions for $\ln K_c$ (K_c: Kielland quotient).

Table 2: Thermodynamic equilibrium constant (K_a) and standard free energy (per equivalent of exchange ions; $\Delta G_a°$) for $2Na^+ \rightarrow Me^{2+}$ exchange on alkali brick (with $Me^{2+} = Cd^{2+}$, Ni^{2+}, Fe^{2+} and Pb^{2+}). And comparison with literature data.

Table 3: Thermodynamic equilibrium constant (K_a^*) and standard free energy (ΔG_a*) for $Me1^{2+} \rightarrow Me2^{2+}$ exchange on alkali brick (with $Me^{2+} = Cd^{2+}$, Ni^{2+}, Fe^{2+} and Pb^{2+}).

Table 4: Radius, R_i, of cationic metals and their spherical shell, ΔR_{H2O}, according to Marcus [71]; Pseudo-second-order kinetic rates (k_2), and initial adsorption rate (r_o), for metals

removals by brick-derived zeolites [45]; The initial adsorption rate (r_o) [45]; The late-stage adsorption rate constant (k_e) [45]; The film diffusion coefficient, D_1, and pore diffusion coefficient, D_2 [45]; The surface diffusion coefficient (Ds) [45].

Table 5: Ionic potential of cationic metal ((Z/R_H); Hydration free energy of metal ion (ΔG_H); Solvation ($\Delta G_{solv,\ Me2+}$) and non-solvation ($\Delta G_{n,Me2+}$) energies.

Figure captions

Figure 1: XRD patterns of raw brick (**A**) and alkali brick (**B**). ***I****, illite;* ***Q****, quartz;* ***R****, rutile;* **(★)**, *NaP zeolite;* **(O)**, *LTA zeolite.*

Figure 2: ESEM image of raw brick (**A**); Elemental ESEM/EDS mapping images (O, Si, Al, K and Fe) and reconstituted ESEM/EDS mapping image (**B**). *BSE: Energy Selected Backscatter.*

Figure 3: ESEM images of NaOH-treated brick showing: *(i)* targeted zones for elemental EDS analysis (**A**); *(ii)* both cubic crystals of NaA zeolite and spherical specimens of NaP zeolite (**B**).

Figure 4: Typical EDS spectrum of targeted brick zones represented in Fig 3A.

Figure 5: Mesopore size distributions on surfaces of brick samples. (**a**) raw brick; (**b**) alkali brick.

Figure 6: Breakthrough curve for the adsorption of Ni^{2+} ions onto alkali brick; Variations of the effluent pH (in red) and the concentration of column Na released in the solution (in blue) *versus* the effluent volume.

Figure 7: Evolution of the content of sodium (which was released in the effluent during the course of the ion-exchange process occurring in fixed-bed column) as a function of the amount of nickel bound to the brick with time.

Figure 8: Ion-exchange isotherms of cationic metals (Cd^{2+}, Fe^{2+}, Ni^{2+} and Pb^{2+}) in alkali-brick suspensions at room temperature.

Figure 9: Competitive ion-exchanges in binary metals systems: Cd-Pb (**a**), Ni-Pb (**b**) and Ni-Cd (**c**); and in a tertiary metals system: Ni-Cd-Pb (**d**).

Figure 10: ***Kielland plots***:The logarithm of the Kielland quotient (K_c) as a function of the equivalent ionic fraction of cationic metal on the alkali brick $(X_{Me})_z$.

Figure 11: Correlation analyses between the thermodynamic equilibrium constant (K_a) for the $2Na^+ \rightarrow Me^{2+}$ exchange on alkali brick and the ionic characteristics of metals (hydrated radius, $R_{H.}$; ion potential, Z/R_H ; hydration free energy, ΔG_H). The curve showing the evolution of the pseudo-second-order rate constant (k_2) *versus* the K_a constant is also given in this figure.

Figure 12: Correlation analyses between the thermodynamic equilibrium constant (K_a) for the $2Na^+ \rightarrow Me^{2+}$ exchange on alkali brick and the the initial adsorption rate (r_o), the late-stage

adsorption rate constant (k_e), the diffusion coefficient (both the film diffusion coefficient, D_1, and pore diffusion coefficient, D_2) and the surface diffusion coefficient (Ds).

Figure captions

Figure 1: XRD patterns of raw brick (**A**) and alkali brick (**B**). ***I****, illite;* ***Q****, quartz;* ***R****, rutile;* **(★)**, *NaP zeolite;* **(O)**, *LTA zeolite*.

Figure 2: ESEM image of raw brick (**A**); Elemental ESEM/EDS mapping images (O, Si, Al, K and Fe) and reconstituted ESEM/EDS mapping image (**B**). *BSE: Energy Selected Backscatter*.

Figure 3: ESEM images of NaOH-treated brick showing: *(i)* targeted zones for elemental EDS analysis (**A**); *(ii)* both cubic crystals of NaA zeolite and spherical specimens of NaP zeolite (**B**).

Figure 4: Typical EDS spectrum of targeted brick zones represented in Fig 3A.

Figure 5: Mesopore size distributions on surfaces of brick samples. (**a**) raw brick; (**b**) alkali brick.

Figure 6: Breakthrough curve for the adsorption of Ni^{2+} ions onto alkali brick; Variations of the effluent pH (in red) and the concentration of column Na released in the solution (in blue) *versus* the effluent volume.

Figure 7: Evolution of the content of sodium (which was released in the effluent during the course of the ion-exchange process occurring in fixed-bed column) as a function of the amount of nickel bound to the brick with time.

Figure 8: Ion-exchange isotherms of cationic metals (Cd^{2+}, Fe^{2+}, Ni^{2+} and Pb^{2+}) in alkali-brick suspensions at room temperature.

Figure 9: Competitive ion-exchanges in binary metals systems: Cd-Pb (**a**), Ni-Pb (**b**) and Ni-Cd (**c**); and in a tertiary metals system: Ni-Cd-Pb (**d**).

Figure 10: ***Kielland plots***:The logarithm of the Kielland quotient (K_c) as a function of the equivalent ionic fraction of cationic metal on the alkali brick $(X_{Me})_z$.

Figure 11: Correlation analyses between the thermodynamic equilibrium constant (K_a) for the $2Na^+ \rightarrow Me^{2+}$ exchange on alkali brick and the ionic characteristics of metals (hydrated radius, $R_{H.}$; ion potential, Z/R_H ; hydration free energy, ΔG_H). The curve showing the evolution of the pseudo-second-order rate constant (k_2) *versus* the K_a constant is also given in this figure.

Figure 12: Correlation analyses between the thermodynamic equilibrium constant (K_a) for the $2Na^+ \rightarrow Me^{2+}$ exchange on alkali brick and the the initial adsorption rate (r_o), the late-stage adsorption rate constant (k_e), the diffusion coefficient (both the film diffusion coefficient, D_1, and pore diffusion coefficient, D_2) and the surface diffusion coefficient (Ds).

FIGURE 1

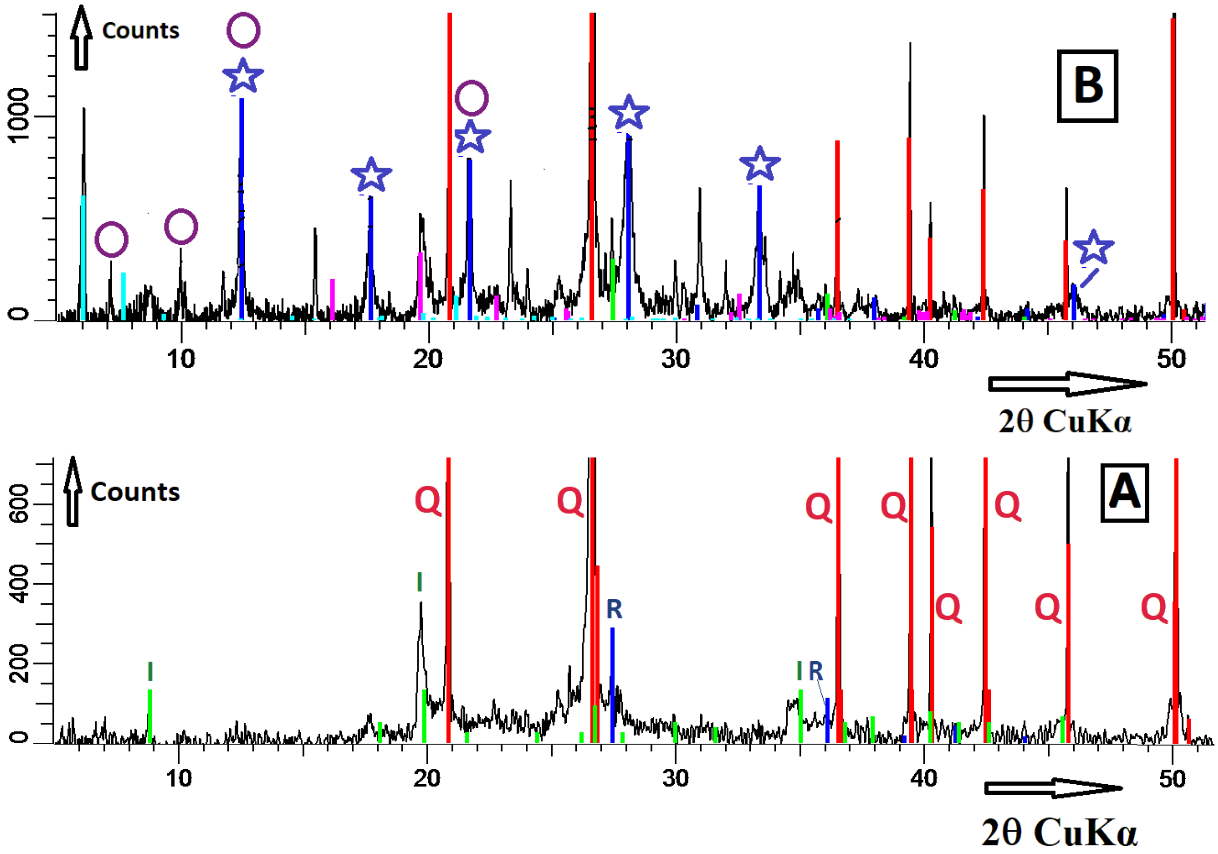
Counts
1000
0
B
10
20
30
40
50
2θ CuKα
Counts
600
400
200
0
A
Q
Q
Q
Q
Q
Q
Q
Q
I
I
I
R
R
10
20
30
40
50
2θ CuKα

FIGURE 2

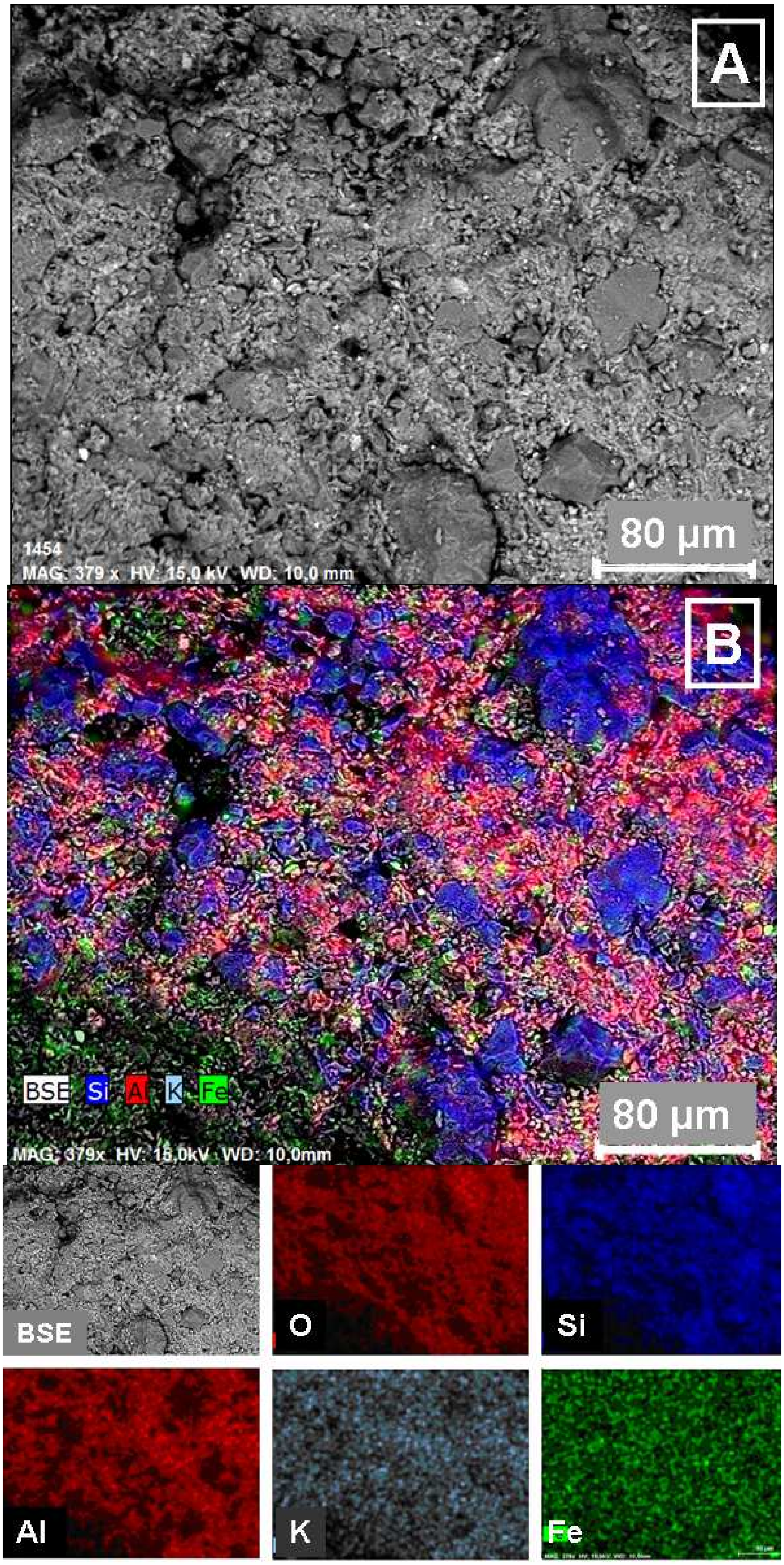
A
1454
MAG: 379 x HV: 15,0 kV WD: 10,0 mm
80 µm
B
BSE Si Al K Fe
80 µm
MAG: 379x HV: 15,0kV WD: 10,0mm
BSE
O
Si
Al
K
Fe

FIGURE 3

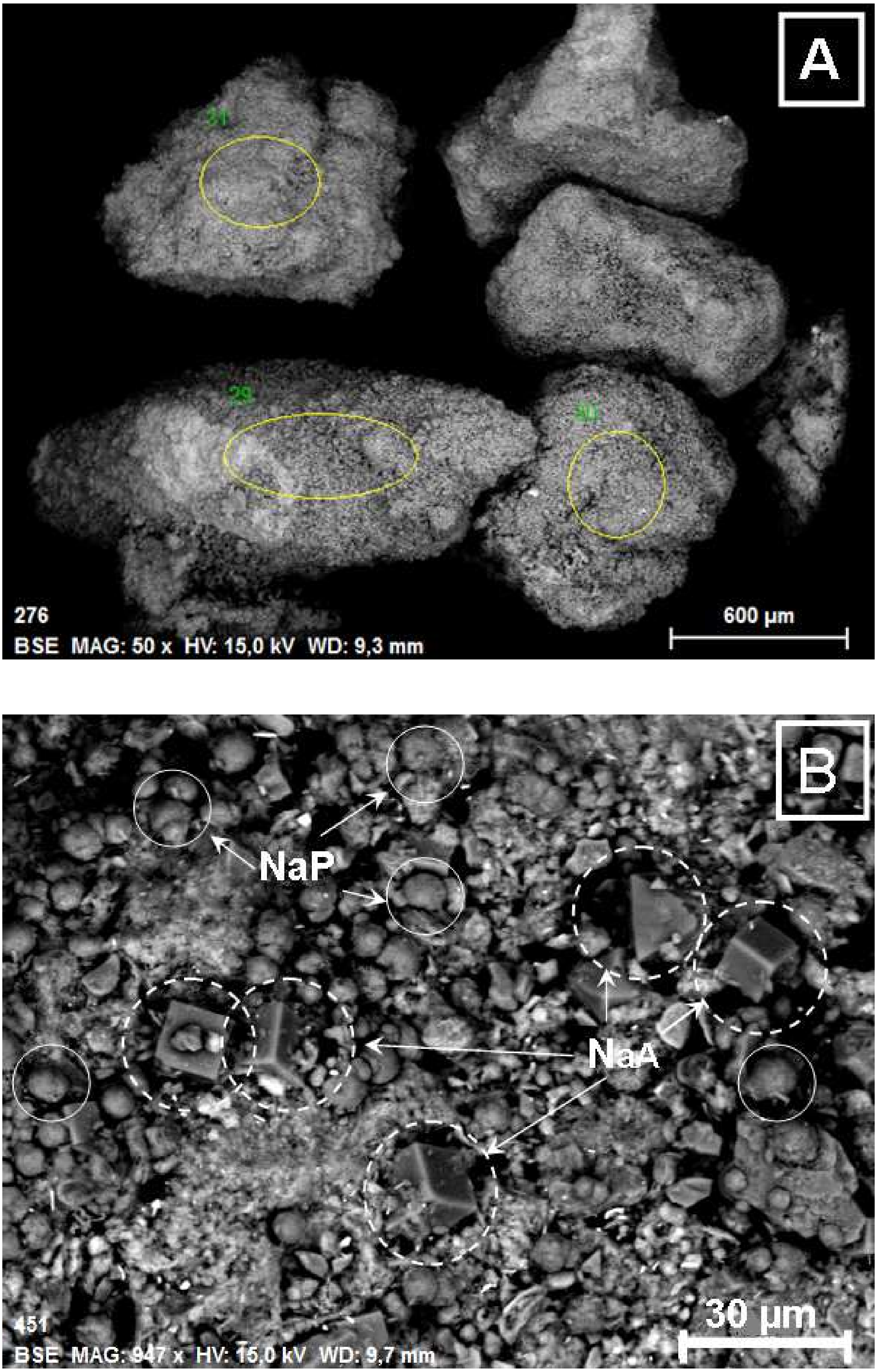
A
31
29
30
276
BSE MAG: 50 x HV: 15,0 kV WD: 9,3 mm
600 µm
B
NaP
NaA
451
BSE MAG: 947 x HV: 15,0 kV WD: 9,7 mm
30 µm

FIGURE 4

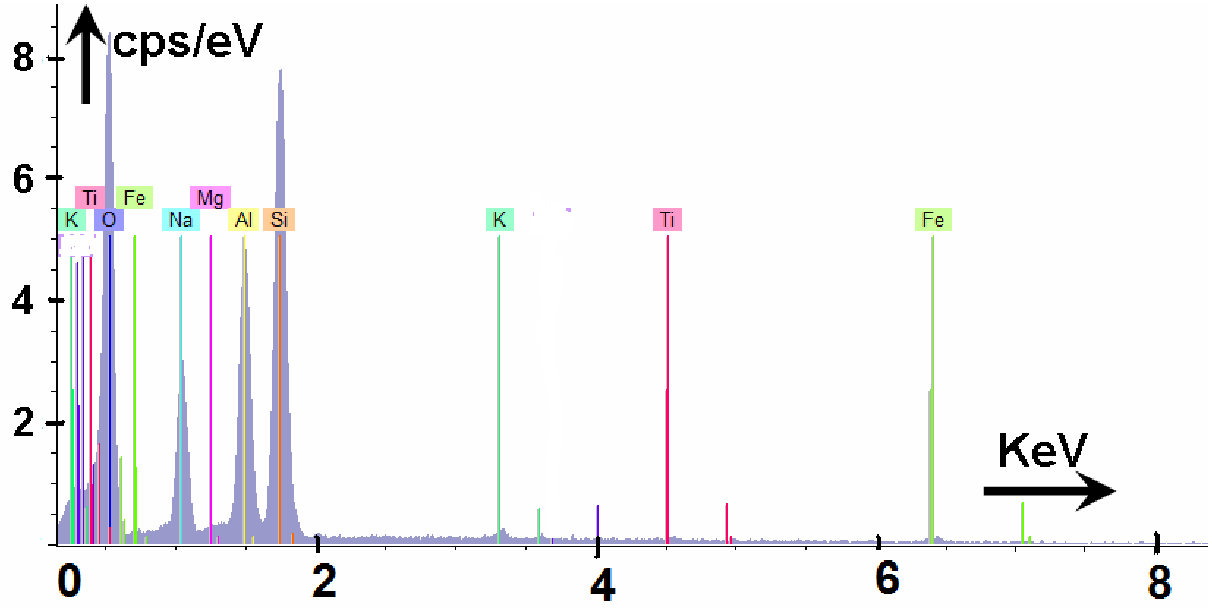

FIGURE 5

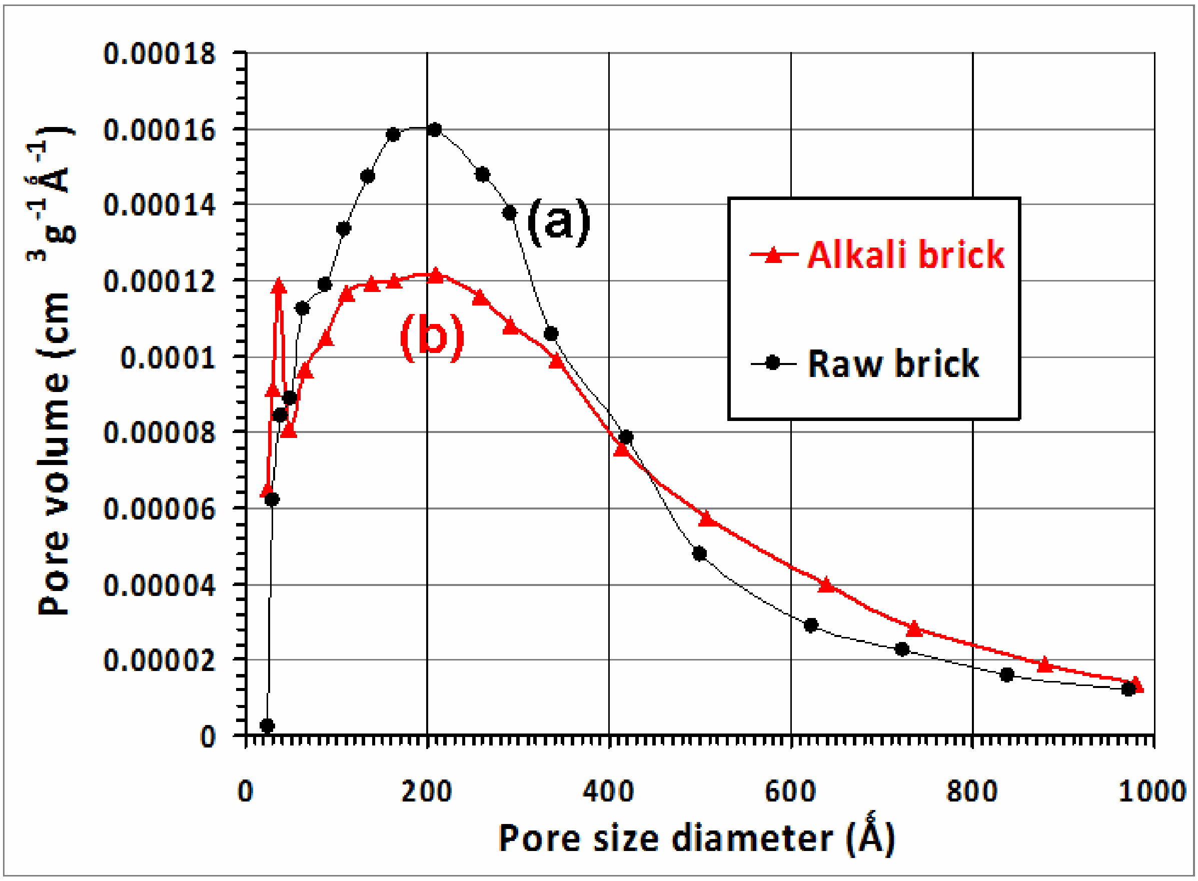
Pore volume (cm^3 g^{-1} Å^{-1})
0.00018
0.00016
0.00014
0.00012
0.0001
0.00008
0.00006
0.00004
0.00002
0
0
200
400
600
800
1000
Pore size diameter (Å)
(a)
(b)
Alkali brick
Raw brick

FIGURE 6

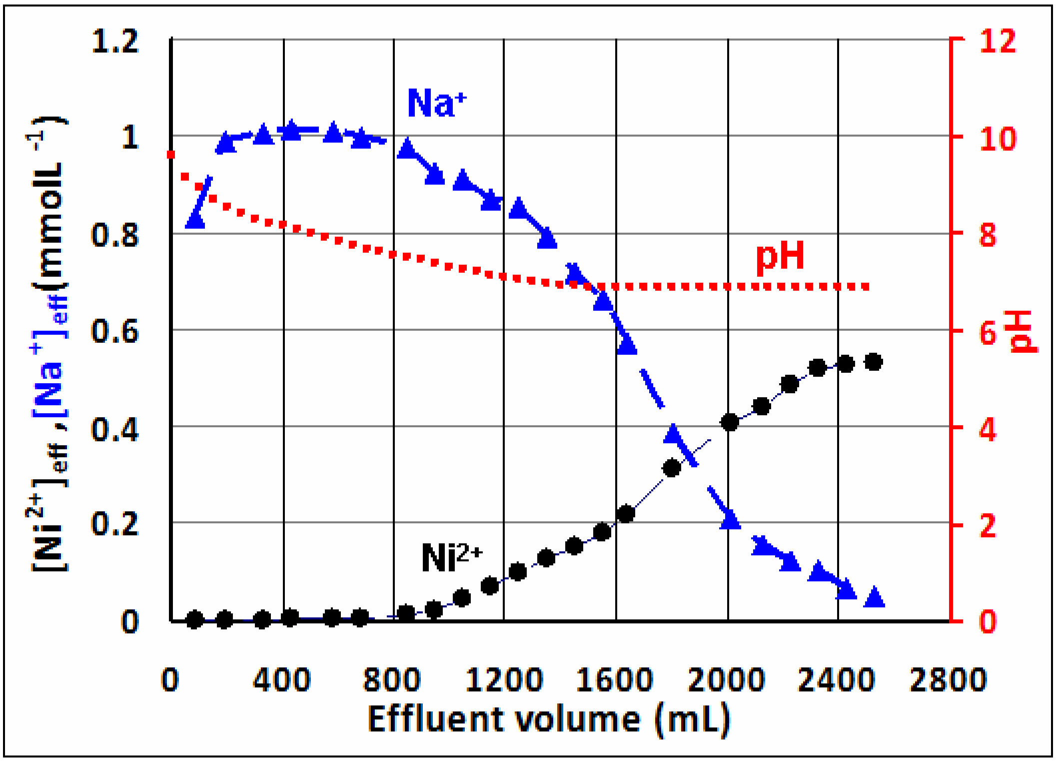

1.2
1
0.8
0.6
0.4
0.2
0
$[Ni^{2+}]_{eff}$,$[Na^{+}]_{eff}$(mmolL $^{-1}$)
Na⁺
pH
Ni²⁺
12
10
8
6
4
2
0
pH
0
400
800
1200
1600
2000
2400
2800
Effluent volume (mL)

FIGURE 7

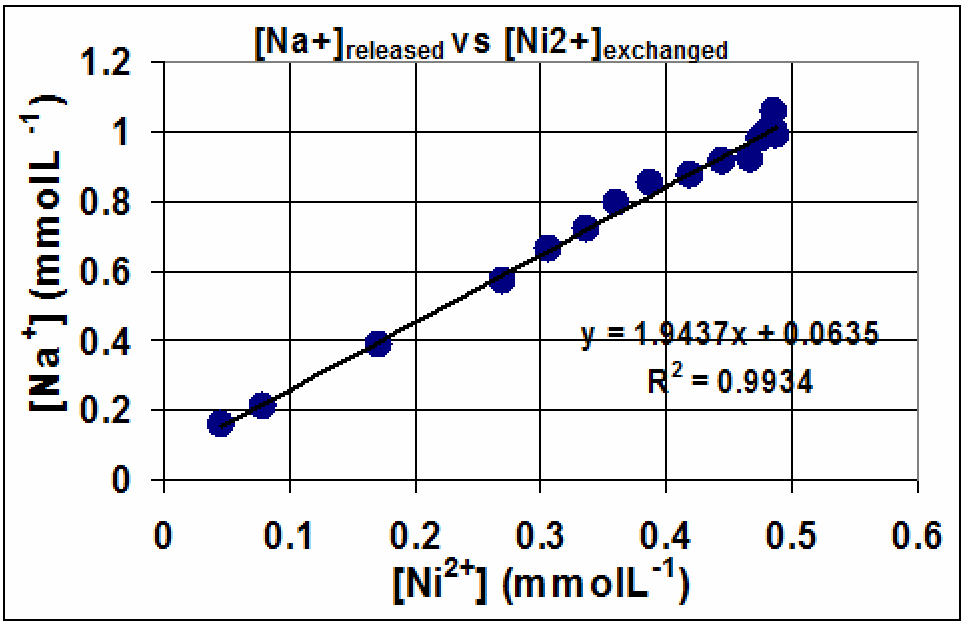
[Na+]released vs [Ni2+]exchanged
1.2
1
0.8
0.6
0.4
0.2
0
[Na+] (mmolL -1)
0
0.1
0.2
0.3
0.4
0.5
0.6
[Ni2+] (mmolL-1)
y = 1.9437x + 0.0635
R2 = 0.9934

FIGURE 8

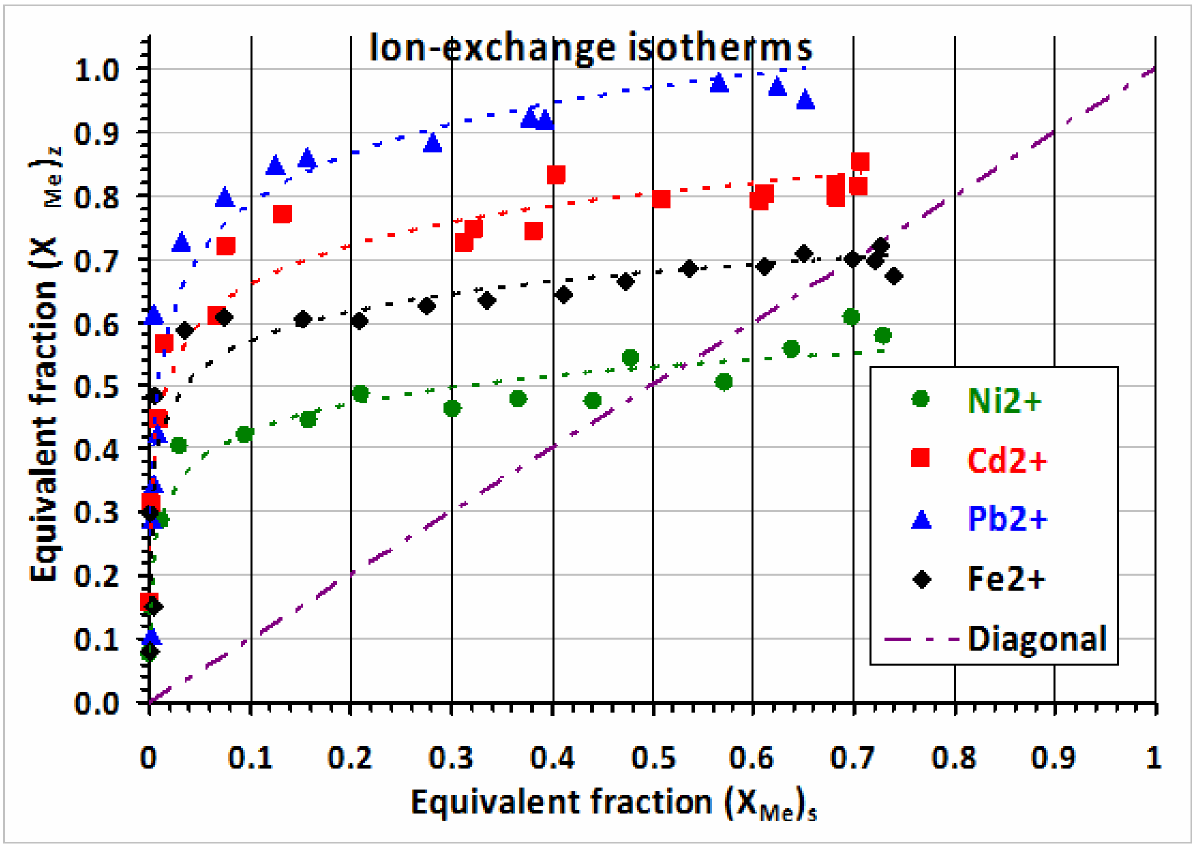
Ion-exchange isotherms
Equivalent fraction ($(X_{Me})_z$)
1.0
0.9
0.8
0.7
0.6
0.5
0.4
0.3
0.2
0.1
0.0
0
0.1
0.2
0.3
0.4
0.5
0.6
0.7
0.8
0.9
1
Equivalent fraction ($(X_{Me})_s$)
Ni2+
Cd2+
Pb2+
Fe2+
Diagonal

FIGURE 9

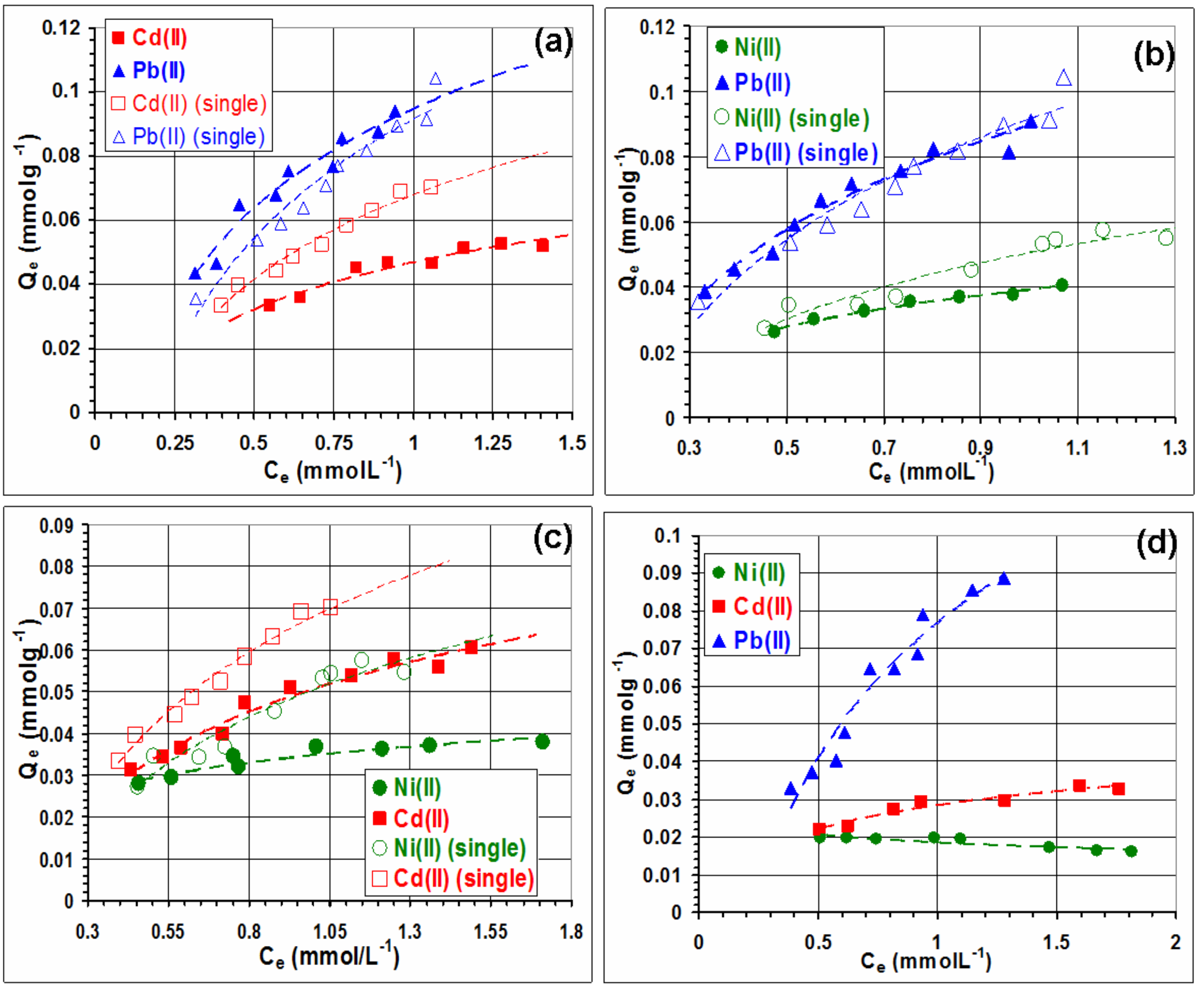
(a)
Cd(II)
Pb(II)
Cd(II) (single)
Pb(II) (single)
0.12
0.1
0.08
0.06
0.04
0.02
0
Qe (mmolg-1)
0
0.25
0.5
0.75
1
1.25
1.5
Ce (mmolL-1)
(b)
Ni(II)
Pb(II)
Ni(II) (single)
Pb(II) (single)
0.12
0.1
0.08
0.06
0.04
0.02
0
Qe (mmolg-1)
0.3
0.5
0.7
0.9
1.1
1.3
Ce (mmolL-1)
(c)
Ni(II)
Cd(II)
Ni(II) (single)
Cd(II) (single)
0.09
0.08
0.07
0.06
0.05
0.04
0.03
0.02
0.01
0
Qe (mmolg-1)
0.3
0.55
0.8
1.05
1.3
1.55
1.8
Ce (mmol/L-1)
(d)
Ni(II)
Cd(II)
Pb(II)
0.1
0.09
0.08
0.07
0.06
0.05
0.04
0.03
0.02
0.01
0
Qe (mmolg-1)
0
0.5
1
1.5
2
Ce (mmolL-1)

FIGURE 10

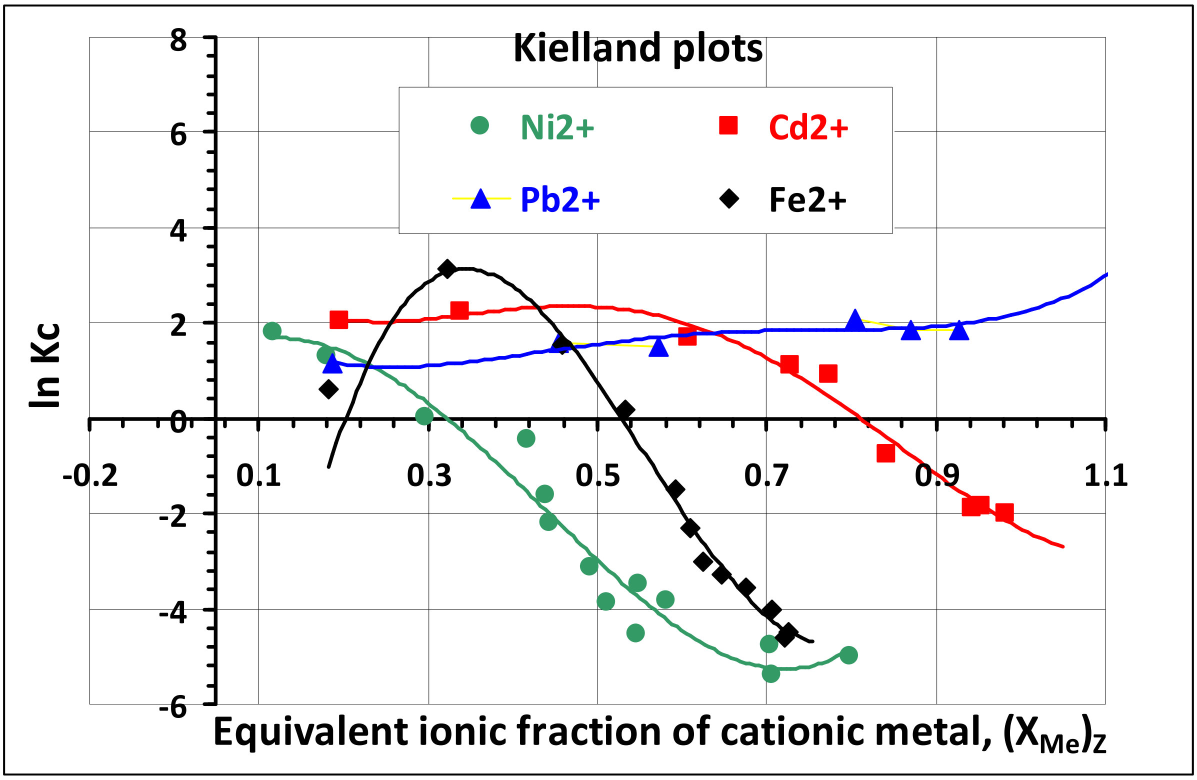
Kielland plots
Ni2+
Cd2+
Pb2+
Fe2+
ln Kc
8
6
4
2
0
-2
-4
-6
-0.2
0.1
0.3
0.5
0.7
0.9
1.1
Equivalent ionic fraction of cationic metal, $(X_{Me})_Z$

FIGURE 11

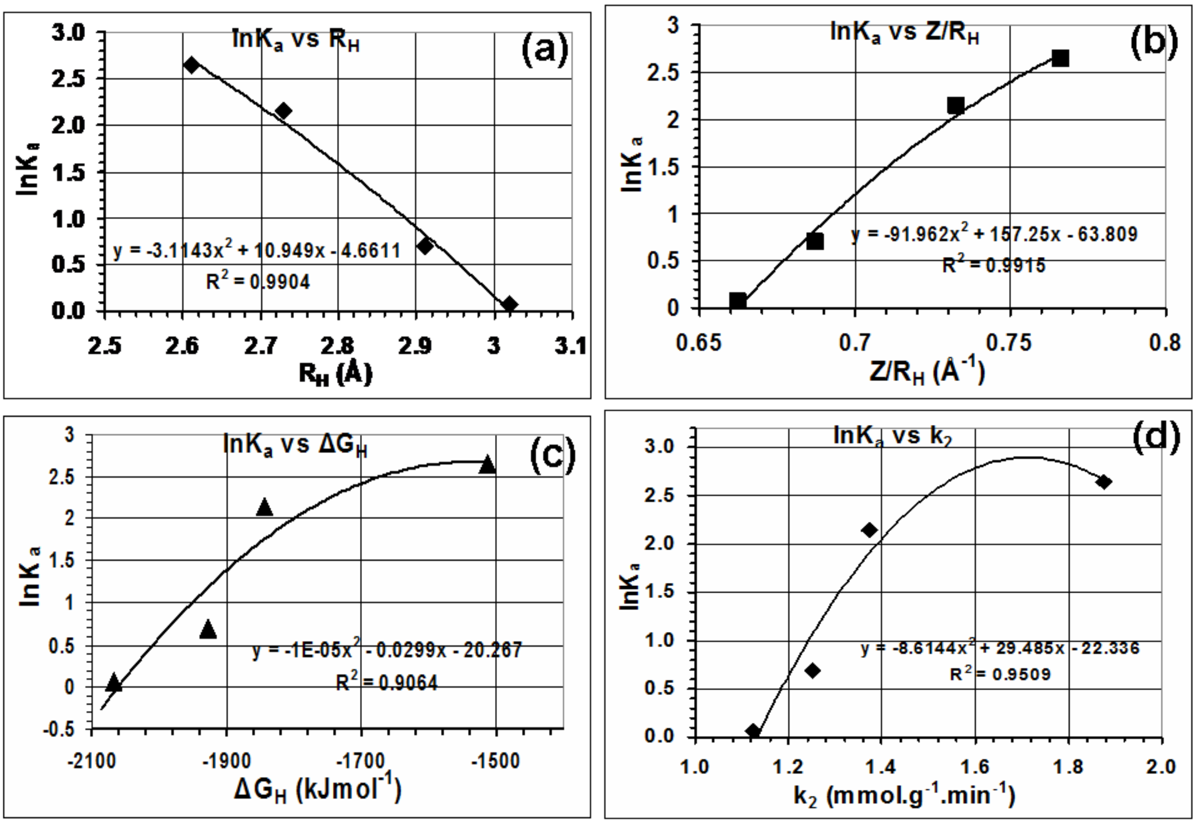
lnKa vs RH
(a)
lnKa
3.0
2.5
2.0
1.5
1.0
0.5
0.0
y = -3.1143x2 + 10.949x - 4.6611
R2 = 0.9904
2.5
2.6
2.7
2.8
2.9
3
3.1
RH (Å)
lnKa vs Z/RH
(b)
lnKa
3
2.5
2
1.5
1
0.5
0
y = -91.962x2 + 157.25x - 63.809
R2 = 0.9915
0.65
0.7
0.75
0.8
Z/RH (Å-1)
lnKa vs ΔGH
(c)
lnKa
3
2.5
2
1.5
1
0.5
0
-0.5
y = -1E-05x2 - 0.0299x - 20.267
R2 = 0.9064
-2100
-1900
-1700
-1500
ΔGH (kJmol-1)
lnKa vs k2
(d)
lnKa
3.0
2.5
2.0
1.5
1.0
0.5
0.0
y = -8.6144x2 + 29.485x - 22.336
R2 = 0.9509
1.0
1.2
1.4
1.6
1.8
2.0
k2 (mmol.g-1.min-1)

FIGURE 12

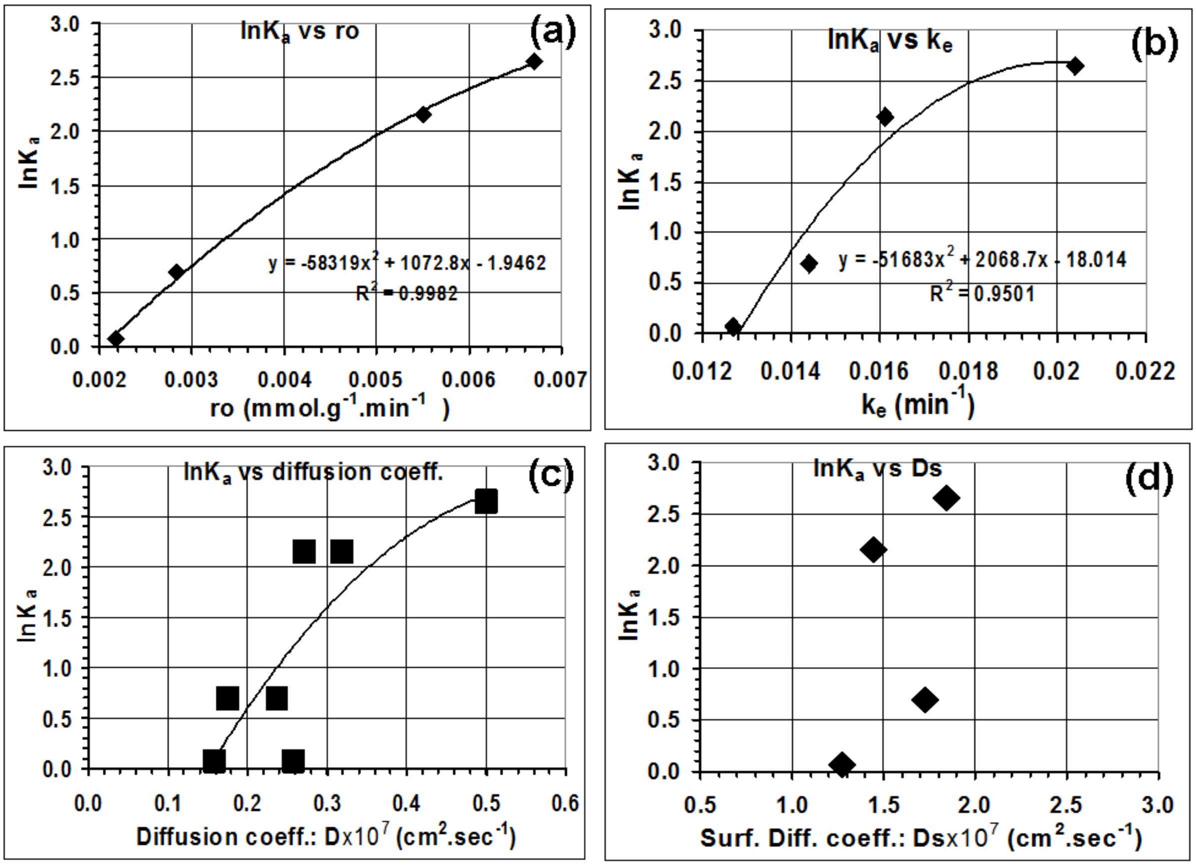
(a)
lnK$_a$ vs ro
lnK$_a$
3.0
2.5
2.0
1.5
1.0
0.5
0.0
0.002
0.003
0.004
0.005
0.006
0.007
ro (mmol.g^{-1}.min^{-1})
y = -58319x^2 + 1072.8x - 1.9462
R^2 = 0.9982
(b)
lnK$_a$ vs k$_e$
lnK$_a$
3.0
2.5
2.0
1.5
1.0
0.5
0.0
0.012
0.014
0.016
0.018
0.02
0.022
k$_e$ (min^{-1})
y = -51683x^2 + 2068.7x - 18.014
R^2 = 0.9501
(c)
lnK$_a$ vs diffusion coeff.
lnK$_a$
3.0
2.5
2.0
1.5
1.0
0.5
0.0
0.0
0.1
0.2
0.3
0.4
0.5
0.6
Diffusion coeff.: Dx10^7 (cm^2.sec^{-1})
(d)
lnK$_a$ vs Ds
lnK$_a$
3.0
2.5
2.0
1.5
1.0
0.5
0.0
0.5
1.0
1.5
2.0
2.5
3.0
Surf. Diff. coeff.: Dsx10^7 (cm^2.sec^{-1})

Table captions

Table 1: $2Na^+ \rightarrow Me^{2+}$ exchanges on alkali brick and polynomial expressions for $\ln K_c$ (K_c: Kielland quotient).

Table 2: Thermodynamic equilibrium constant (K_a) and standard free energy (per equivalent of exchange ions; $\Delta G_a°$) for $2Na^+ \rightarrow Me^{2+}$ exchange on alkali brick (with $Me^{2+} = Cd^{2+}$, Ni^{2+}, Fe^{2+} and Pb^{2+}). And comparison with literature data.

Table 3: Thermodynamic equilibrium constant (K_a^*) and standard free energy (ΔG_a*) for $Me1^{2+} \rightarrow Me2^{2+}$ exchange on alkali brick (with $Me^{2+} = Cd^{2+}$, Ni^{2+}, Fe^{2+} and Pb^{2+}).

Table 4: Radius, R_i, of cationic metals and their spherical shell, ΔR_{H2O}, according to Marcus [71]; Pseudo-second-order kinetic rates (k_2), and initial adsorption rate (r_o), for metals removals by brick-derived zeolites [45]; The initial adsorption rate (r_o) [45]; The late-stage adsorption rate constant (k_e) [45]; The film diffusion coefficient, D_1, and pore diffusion coefficient, D_2 [45]; The surface diffusion coefficient (Ds) [45].

Table 5: Ionic potential of cationic metal ((Z/R_H); Hydration free energy of metal ion (ΔG_H); Solvation ($\Delta G_{solv, Me2+}$) and non-solvation ($\Delta G_{n,Me2+}$) energies.

TABLE 1

Ion Exchanges	**Polynomial expressions __with $x = (X_{Me})_z$__**	**R^2**	**Integral term of Eq.(7)**
$2Na^+ \rightarrow Cd^{2+}$	$+3.5086-19.247x^1 +82.109x^2-125.85x^3+56.788x^4$	0.9821	+1.1499
$2Na^+ \rightarrow Fe^{2+}$	$-8.1463+94.765x^1 -230.59x^2-149.28x^3+0.00x^4$	0.9891	-0.3071
$2Na^+ \rightarrow Ni^{2+}$	$+1.4917+7.6148x^1 -50.919x^2+21.358x^3+26.995x^4$	0.9444	-0.9354
$2Na^+ \rightarrow Pb^{2+}$	$+2.2244-13.387x^1 +50.599x^2-67.352x^3+30.44x^4$	0.9515	+1.6472

TABLE 2

Cationic metals		**Cd^{2+}**	**Fe^{2+}**	**Ni^{2+}**	**Pb^{2+}**
$\ln K_a$	*This work*	2.149(9)	0.692(9)	0.064(6)	2.647(2)
	Ref.[58]§	2.27	---------	0.985	2.60
	Ref.[59](a)	-3.689(a)	---------	---------	3.126(8)(a)
	Ref.[59](b)	-0.562(b)	---------	---------	1.411(b)
	Ref.[59](c)	-1.772(c)			0.285(c)
	Ref.[62](d)				2.81(d)
	Ref.[63](e)	---------	---------	1.80(e)	---------
ΔG^o_a ($kJeq^{-1}$)	*This work*	-2.663	-0.858	-0.080	-3.279
	Ref.[58]§	-2.810	---------	-1.22	-3.225
	Ref.[59](a)	+4.570(a)	---------	---------	-3.873(a)
	Ref.[59](b)	+0.696(b)	---------	---------	-1.748(b)
	Ref.[59](c)	+2.195(c)	--------	---------	-0.353(c)
	Ref.[62](d)				-3.81(d)
	Ref.[63](e)	---------	---------	-2.22(e)	---------

§: LTA zeolites [58].. (a): Italian natural phillipsites of sedimentary origin with Si/Al =2.39- 2.47 [59]; (b): Italian natural chabazites of sedimentary origin with Si/Al =2.44-2.54 [59]; (c): Italian natural clinoptilolites of sedimentary origin with Si/Al = 4.17 [59]; (d): Western Anatolia clinoptilolite (Turkey) [62]; (e): Cuban clinoptilolite modified to its ammonium form [63].

TABLE 3

Ion exchanges	**$Ni^{2+} \rightarrow Cd^{2+}$**	**$Ni^{2+} \rightarrow Fe^{2+}$**	**$Ni^{2+} \rightarrow Pb^{2+}$**	**$Cd^{2+} \rightarrow Pb^{2+}$**
$\ln K_a^*$	+2.085(3)	+0.622(3)	+2.582(6)	+0.497(3)
ΔG_a^* (kJmol^{-1})	-5.167	-1.542	-6.399	-1.232

TABLE 4

Cationic metals	**Cd^{2+}**	**Fe^{2+}**	**Ni^{2+}**	**Pb^{2+}**
R_{Me2+} (Å)*	0.95	0.78	0.69	1.18
ΔR_{H2O} (Å)*	1.78	2.13	2.33	1.43
R_{Total} (Å)§	2.73	2.91	3.02	2.61
Z/R_H (Å^{-1}) (Z=+2)	0.7326	0.6873	0.6623	0.7663
k_2 (mmol. g^{-1}.min^{-1})§	1.3743	1.2505	1.1231	1.8753
r_o (mmol. g^{-1}.min^{-1})§	$5.50.10^{-3}$	$2.84.10^{-3}$	$2.17.10^{-3}$	$6.71.10^{-3}$
k_e (min^{-1})	0.0161	0.0144	0.0127	0.0204
From Crank-Reichenberg Eq. **D_1 (cm^{2}sec^{-1})§**	$3.20.10^{-8}$	$2.38.10^{-8}$	$2.58.10^{-8}$	$5.00.10^{-8}$
D_2 (cm^{2}sec^{-1})§	$2.272.10^{-7}$	$1.770.10^{-7}$	$1.588.10^{-7}$	$1.759.10^{-7}$
UsingYao-Chen approxi. **Ds (cm^{2}sec^{-1})§**	$1.448.10^{-7}$	$1.726.10^{-7}$	$1.274.10^{-7}$	$1.845.10^{-7}$

* see ref. [71]; § see ref. [45]; $R_{Total} = R_H$.

TABLE 5

Cationic metals	**Ionic potential**[a] **(Å^{-1})**	**Hydration free energy, ΔG_H** [b] **(kJmol^{-1})**	**$\Delta G_{solv.,Me2+}$** [c] **(kJmol^{-1})**	**$\Delta G_{n,Me2+}$** [c] **(kJmol^{-1})**
Cd^{2+}	0.7326	-1843	-517.84	446.90
Fe^{2+}	0.6873	-1928	-594.46	498.94
Ni^{2+}	0.6623	-2068	-622.78	573.00
Pb^{2+}	0.7663	-1513	-451.74	427.52

[a]**:** Ionic potential defined as the ratio Z/R_H, where Z is the charge of the cation and R_H is the hydrated radius calculated according to the Marcus's method [71]; [b] **:** Hydration free energy (ΔG_H) reported by Kepp [77]; [c]**:** Solvation ($\Delta G_{solv.,Me2+}$) and non-solvation energy ($\Delta G_{n,Me2+}$) reported by Torres and Gubulin [78].

GRAPHICAL ABSTRACT